Universiteit Leiden
The Netherlands

NUDCD3 deficiency disrupts V(D)J recombination to cause SCID and Omenn syndrome

Chen, R.; Lukianova, E.; Loeff, I.S. van der; Spegarova, J.S.; Willet, J.D.P.; James, K.D.; ... ; Hambleton, S.

Citation
Chen, R., Lukianova, E., Loeff, I. S. van der, Spegarova, J. S., Willet, J. D. P., James, K. D., … Hambleton, S. (2024). NUDCD3 deficiency disrupts V(D)J recombination to cause SCID and Omenn syndrome. *Science Immunology*, *9*(95). doi:10.1126/sciimmunol.ade5705

Version:	Publisher's Version
License:	Licensed under Article 25fa Copyright Act/Law (Amendment Taverne)
Downloaded from:	https://hdl.handle.net/1887/4283209

Note: To cite this publication please use the final published version (if applicable).

Check for updates

IMMUNODEFICIENCY

Copyright © 2024 The Authors, some rights reserved; exclusive licensee American Association for the Advancement of Science. No claim to original U.S. Government Works

NUDCD3 deficiency disrupts V(D)J recombination to cause SCID and Omenn syndrome

Rui Chen[1]†, Elena Lukianova[2]†, Ina Schim van der Loeff[1,3], Jarmila Stremenova Spegarova[1], Joseph D.P. Willet[1], Kieran D. James[4], Edward J. Ryder[2], Helen Griffin[1], Hanna IJspeert[5], Akshada Gajbhiye[6], Frederic Lamoliatte[6]‡, Jose L. Marin-Rubio[6]§, Lisa Woodbine[7], Henrique Lemos[1], David J. Swan[1]¶, Valeria Pintar[1], Kamal Sayes[1], Elias R. Ruiz-Morales[2], Simon Eastham[2]#, David Dixon[6], Martin Prete[2], Elena Prigmore[2], Penny Jeggo[7], Joan Boyes[8], Andrew Mellor[1], Lei Huang[1], Mirjam van der Burg[5], Karin R. Engelhardt[1], Asbjørg Stray-Pedersen[9], Hans Christian Erichsen[10], Andrew R. Gennery[1,3], Matthias Trost[6], David J. Adams[2], Graham Anderson[4], Anna Lorenc[2], Gosia Trynka[2,11], Sophie Hambleton[1,3]***

Inborn errors of T cell development present a pediatric emergency in which timely curative therapy is informed by molecular diagnosis. In 11 affected patients across four consanguineous kindreds, we detected homozygosity for a single deleterious missense variant in the gene NudC domain–containing 3 (*NUDCD3*). Two infants had severe combined immunodeficiency with the complete absence of T and B cells (T$^-$B$^-$ SCID), whereas nine showed classical features of Omenn syndrome (OS). Restricted antigen receptor gene usage by residual T lymphocytes suggested impaired V(D)J recombination. Patient cells showed reduced expression of NUDCD3 protein and diminished ability to support RAG-mediated recombination in vitro, which was associated with pathologic sequestration of RAG1 in the nucleoli. Although impaired V(D)J recombination in a mouse model bearing the homologous variant led to milder immunologic abnormalities, NUDCD3 is absolutely required for healthy T and B cell development in humans.

INTRODUCTION

The molecular dissection of inborn errors of immunity provides powerful insights into genes and pathways of nonredundant importance to the human immune system. Nowhere is this truer than in severe combined immunodeficiency (SCID), a failure of T cell development that leaves affected infants exceptionally vulnerable to infection (*1*). Genes associated with SCID highlight the critical role of T cell receptor (TCR) rearrangement and signaling, alongside survival signals via the interleukin 7 receptor (IL-7R) during T lymphocyte development (*2*). Omenn syndrome (OS) is a related disorder, in which an incomplete developmental block allows the dysregulated expansion of oligoclonal T cells, causing inflammation of the skin and viscera as well as SCID-like susceptibility to infection (*3*). Because these conditions are both treatable and life threatening, many nations have recently introduced newborn screening for T cell immunodeficiency (*4*). In affected infants, a specific molecular diagnosis may guide precision medicine such as enzyme replacement, gene therapy, or hematopoietic stem cell transplantation (HSCT) (*1*).

OS is particularly associated with disorders of V(D)J recombination, the complex process whereby antigen receptor loci are rearranged to produce functional TCR and immunoglobulin genes (*5*). Although this process is absolutely required for the generation of a diverse adaptive immune repertoire, the accompanying introduction and recombinatorial repair of DNA double-strand breaks implies a moment of extreme risk for genome integrity. It is therefore anticipated that V(D)J recombination occurs through specialized molecular machinery, including the T cell– and B cell–specific recombination-activating gene (RAG) recombinases, whose expression and activity are tightly controlled (*6*–*8*).

RESULTS

A homozygous, hypomorphic *NUDCD3* variant in infants with SCID/OS

In this study, we sought to extend knowledge of lymphocyte development by studying patients with classical OS or T$^-$B$^-$ SCID who lacked pathogenic variants in known disease genes, such as those encoding the recombinases RAG1 and RAG2 or components of the DNA-repair machinery including Artemis (*2*, *5*). The occurrence of multiple familial cases within four independent, consanguineous kindreds from the same ethnic (South Asian) background suggested that there was autosomal recessive inheritance of a shared ancestral morbid allele (Fig. 1A and tables S1 and S2). Both family 1 (*9*) and family 2 (*10*) have been previously described. By integrative analysis

[1]Translational and Clinical Research Institute, Newcastle University, NE2 4HH Newcastle upon Tyne, UK. [2]Wellcome Sanger Institute, Wellcome Genome Campus, CB10 1SA Hinxton, UK. [3]Great North Children's Hospital, Newcastle upon Tyne Hospitals NHS Foundation Trust, NE1 4LP Newcastle upon Tyne, UK. [4]Institute of Immunology and Immunotherapy, University of Birmingham. B15 2TT Birmingham, UK. [5]Department of Immunology, Erasmus University Medical Center, Rotterdam 3000 CA, Netherlands. [6]Biosciences Institute, Newcastle University, NE2 4HH Newcastle upon Tyne, UK. [7]Genome Damage and Stability Centre, University of Sussex, BN1 9RQ Brighton, UK. [8]Faculty of Biological Sciences, University of Leeds, LS2 9JT Leeds, UK. [9]Norwegian National Unit for Newborn Screening, Division of Pediatric and Adolescent Medicine, Oslo University Hospital, Oslo 0424, Norway. [10]Division of Pediatric and Adolescent Medicine, Oslo University Hospital and Institute of Clinical Medicine, University of Oslo, Oslo 0424, Norway. [11]Open Targets, Wellcome Genome Campus, CB10 1SA Hinxton, UK.
*Corresponding author. Email: sophie.hambleton@ncl.ac.uk
†These authors contributed equally to this work.
‡Present address: MRC PPU, School of Life Sciences, University of Dundee, DD1 5EH Dundee, UK.
§Present address: Human Oncology and Pathogenesis Program, Memorial Sloan Kettering Cancer Center, New York, NY 10065, USA.
¶Present address: School of Medicine, University of Sunderland, SR1 3SD Sunderland, UK.
#Present address: School of Cellular and Molecular Medicine, University of Bristol, BS8 1TD Bristol, UK.
**Present address: Departments of Pediatrics and Immunology, Leiden University Medical Center, Leiden 2300 RC, Netherlands.

Downloaded from https://www.science.org at Leiden University on November 20, 2025

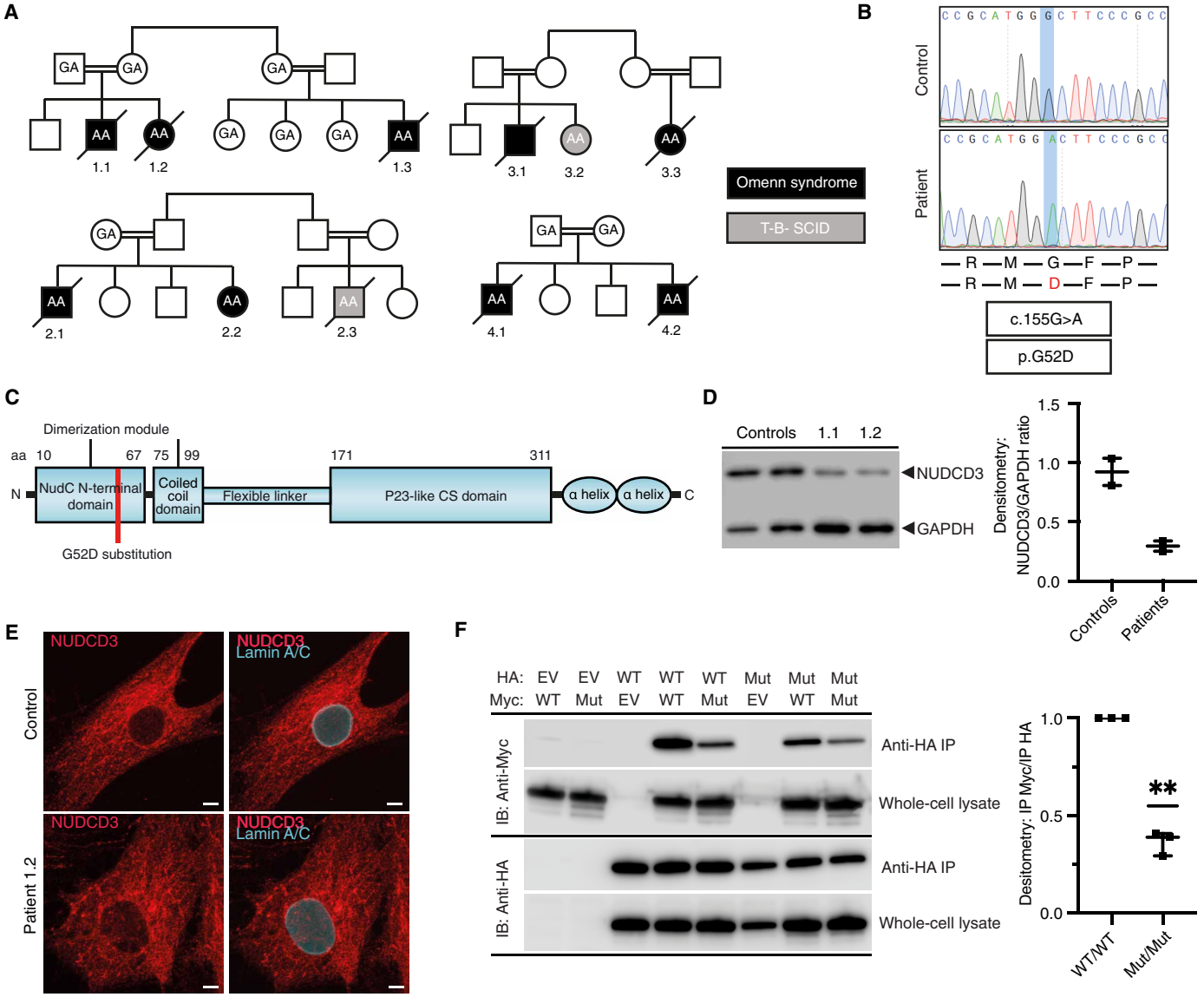

Fig. 1. An autosomal recessive variant in *NUDCD3* causes SCID/OS. (**A**) Pedigrees showing patients affected by OS (black) and T$^-$B$^-$ SCID (gray) with letters indicating genotype. (**B**) Representative Sanger sequencing chromatogram of patient as compared with reference. (**C**) Schematic representation of NUDCD3 protein domains with the location of the G52D substitution highlighted in red. (**D**) Immunoblot showing reduced protein expression of NUDCD3 in primary patient dermal fibroblasts compared with controls (top) with corresponding densitometry analysis (bottom) ($n = 2$, normalized NUDCD3/GAPDH ratio; each data point represents average from each individual). (**E**) Comparable distribution of NUDCD3 (red) in representative immunofluorescence micrographs of healthy control and patient fibroblasts costained with nuclear membrane marker lamin A/C (cyan). Scale bars, 5 μm. (**F**) Impaired dimerization of NUDCD3^{G52D} by comparison with NUDCD3^{WT} upon coimmunoprecipitation with alternatively tagged NUDCD3^{WT} or NUDCD3^{G52D} in HEK293T cells transfected with plasmids encoding corresponding proteins (EV, empty vector; WT, wild type; Mut, G52D variant; IB, immunoblot) (top) and quantified by densitometry (below) (Myc IP/HA IP, ratio to WT/WT, $n = 3$, one-sample t test. Statistical significance was defined as $^{**}P < 0.01$).

of whole-exome sequencing (WES) data, we identified a single homozygous missense variant in the gene *NUDCD3* (NudC domain–containing 3), which segregated with disease in all four affected kindreds but was absent from the gnomAD and Genome Asia databases, in keeping with a rare disease allele (Fig. 1, A and B, and fig. S1) (*11*, *12*). This gene appeared to be intolerant of loss-of-function variation with a LOEUF score (loss-of-function observed/expected upper-bound fraction) of 0.21 and no instances of homozygous predicted null variants in the gnomAD database (fig. S1) (*12*). The missense variant c.155G>A introduced a charge change by substituting aspartate for a glycine residue at position 52 within the highly conserved N-terminal domain of NUDCD3 (Fig. 1C). Programs including combined annotation dependent depletion (CADD, score of 29.9), Polyphen2 (score of 1.0), and VARITY-ER (score of 0.964) predicted that this variant is highly damaging (fig. S1 and table S3) (*13*–*15*).

NUDCD3 is ubiquitously expressed in vertebrates and belongs to the NudC family of p23 domain–containing proteins that exhibit

Downloaded from https://www.science.org at Leiden University on November 20, 2025

cochaperone and intrinsic chaperone activity (*16*). This protein family emerged at the same time as β-propeller structures within increasingly complex multidomain and multisubunit proteins (*17*, *18*). Family members NUDC and NUDCL2 have recently been shown to act as cochaperones in Hsp90-related refolding of client proteins such as the glucocorticoid receptor and cohesin, respectively (*19*, *20*).

NUDCD3 was specifically linked to dynein intermediate chain stability and viability through study of *NUDCD3* knockdown cells in vitro (*21*), whereas its overexpression impaired cytokinesis (*22*). The only prior literature linking NUDCD3 to the immune system reported the appearance of RAG1 among its interactome when assessed by a LUMIER screen of potential client proteins shared with Hsp90 (*18*). The same screen noted a predominance for NUDCD3 of binding partners containing kelch-like domains, such as RAG2, which was, however, not tested in this study (*18*). In addition, our reanalysis of data from developing human embryos confirmed the expression of *NUDCD3* transcripts in the thymus and bone marrow (BM) (*23*, *24*).

NUDCD3 protein expression in patient dermal fibroblasts was reduced relative to control despite equivalent mRNA expression, indicating hypomorphic behavior of the variant allele (Fig. 1D and fig. S2). However, NUDCD3^{G52D} was distributed between the cytoplasm and nucleus in a manner indistinguishable from wild-type (WT) protein, whether endogenously expressed or transfected into cells in tagged form (Fig. 1E and fig. S3).

Patient cells divided normally and did not show significantly impaired resistance to gamma irradiation (fig. S4A). Moreover, *NUDCD3* knockdown did not affect the radiation sensitivity of A549 cells, indicating their preserved ability to repair DNA double-strand breaks (fig. S4B). However, *NUDCD3* is an essential gene in many cell lines, suggesting that homozygosity for a complete null allele would not be viable (*25*).

To compare the global properties of mutant and WT NUDCD3, we prepared mild detergent lysates of transfected cells, separated protein complexes by size exclusion chromatography, and probed the resulting fractions for NUDCD3 after SDS–polyacrylamide gel electrophoresis under denaturing conditions (fig. S4C). Both WT and variant NUDCD3 participated in protein complexes of diverse size to a similar extent. However, coimmunoprecipitation experiments in which distinctively tagged mutant and/or WT *NUDCD3* were cotransfected showed significantly reduced homodimerization potential for the G52D variant (Fig. 1F). Thus, the G52D variant does not grossly alter the physical properties of NUDCD3 but disrupts a specific function of the protein within the immune system, potentially one requiring its dimerization.

NUDCD3^{G52D} patients exhibit defective V(D)J recombination

To gain further insight into pathomechanism, we undertook single-cell studies of cryopreserved peripheral blood mononuclear cells from patients with OS associated with either the *NUDCD3* variant or pathogenic defects of *RAG1* or *RAG2* (tables S4 and S5). Compared with healthy controls, drastic abnormalities in the distribution of circulating lymphocyte subsets were readily observed in patients with OS by flow cytometry, including the complete lack of B cells and naïve T cells (Fig. 2A). Single-cell RNA sequencing (scRNA-seq) revealed widely divergent distribution across the 39 cell subpopulations annotated (32 lymphoid and seven myeloid), including within each of the mutation groups (Fig. 2, B and C). We detected γδ T cells, for example, in only 8 of 11 patients with OS. However, in two of these individuals, γδ T cells constituted more than 20% of total T cells, a much higher proportion than in healthy controls. When present, the CD8$^+$ and γδ T cell compartments were abnormally skewed toward weakly cytotoxic (e.g., lacking *NKG7*, granzymes, granulysin, and chemokines) and non-naïve (e.g., high expression of *IL32* and absence of *CCR7*) phenotypes with low regulatory potential toward T cell and natural killer (NK) cell effectors (Fig. 2C and fig. S5). CD4$^+$ T cells were enriched for central memory and effector memory phenotypes (characterized by high expression of *LGALS1*, *NEAT1*, and *GZMA* as well as cytoskeletal and *HLA* genes) (Fig. 2C and fig. S5). These T cell abnormalities were prominent in both *NUDCD3*- and *RAG*-mutated OS patients, as were associated alterations of the myeloid compartment. The latter included enrichment for classical monocytes distinguished by a cytotoxic, proinflammatory, and chemotactic (*CCL2*) transcriptional signature (fig. S6).

Analysis of TCR gene usage within our single-cell transcriptomic data revealed reduced diversity and expanded clonotype size in patients with OS, as expected (Fig. 2D and fig. S7A). We confirmed the previously noted skewing of the *RAG1/2*-deficient TCR repertoire toward the use of *TRA* gene segments near the 3′ end of the Vα locus and the 5′ end of the Jα locus (Fig. 2E) (*26*), a pattern that was reproduced in the T cells of patients with *NUDCD3*^{G52D} (Fig. 2E). These proximal *TRA* gene segments are preferentially recombined at the start of the DP stage of thymocyte development. If the resulting TCRα chain, alongside the preexisting TCRβ chain, is incapable of self-peptide major histocompatibility complex recognition, then more distal segments are used in subsequent recombination rounds until a productive recombination results in the down-regulation of *RAG1* expression (*27*). The predominance of proximal Vα and Jα gene segment usage therefore implied that *NUDCD3*^{G52D} T cells were unable to execute repeated rounds of V(D)J recombination during their development, just as in RAG Omenn T cells. We confirmed the reduced diversity of TCRβ chain usage in patients with OS without obvious skewing across the *TRB* locus (fig. S7, A and B), consistent with prior literature (*28*, *29*).

These data suggested that there was a primary defect in V(D)J recombination associated with homozygosity for the *NUDCD3*^{G52D} variant. We therefore tested the integrity of RAG-dependent recombination by cotransfecting patient and control fibroblasts with *RAG1*, *RAG2*, and a synthetic substrate for RAG recombination, which could be detected by polymerase chain reaction (PCR) of the rearranged product. In this preliminary screen, where the expression of each transfected component could not be assessed at single-cell level, *NUDCD3*^{G52D} patient cells nonetheless appeared highly defective in supporting RAG-dependent recombination (Fig. 2F). We consequently turned to murine systems in which to model this effect in a more physiological context.

NUDCD3 plays a conserved role in mouse V(D)J recombination

To test whether endogenous V(D)J rearrangement was similarly NUDCD3 dependent, we took advantage of a mouse pre-B cell line, 103/BCL2, in which this process can be triggered by a shift in temperature and detected by quantitative PCR for kappa-deleting recombination excision circles (KRECs) (*30*). Cells in which *Nudcd3* expression had been partially knocked down by small interfering RNA (siRNA) transfection were defective for V(D)J recombination (Fig. 2G).

Downloaded from https://www.science.org at Leiden University on November 20, 2025

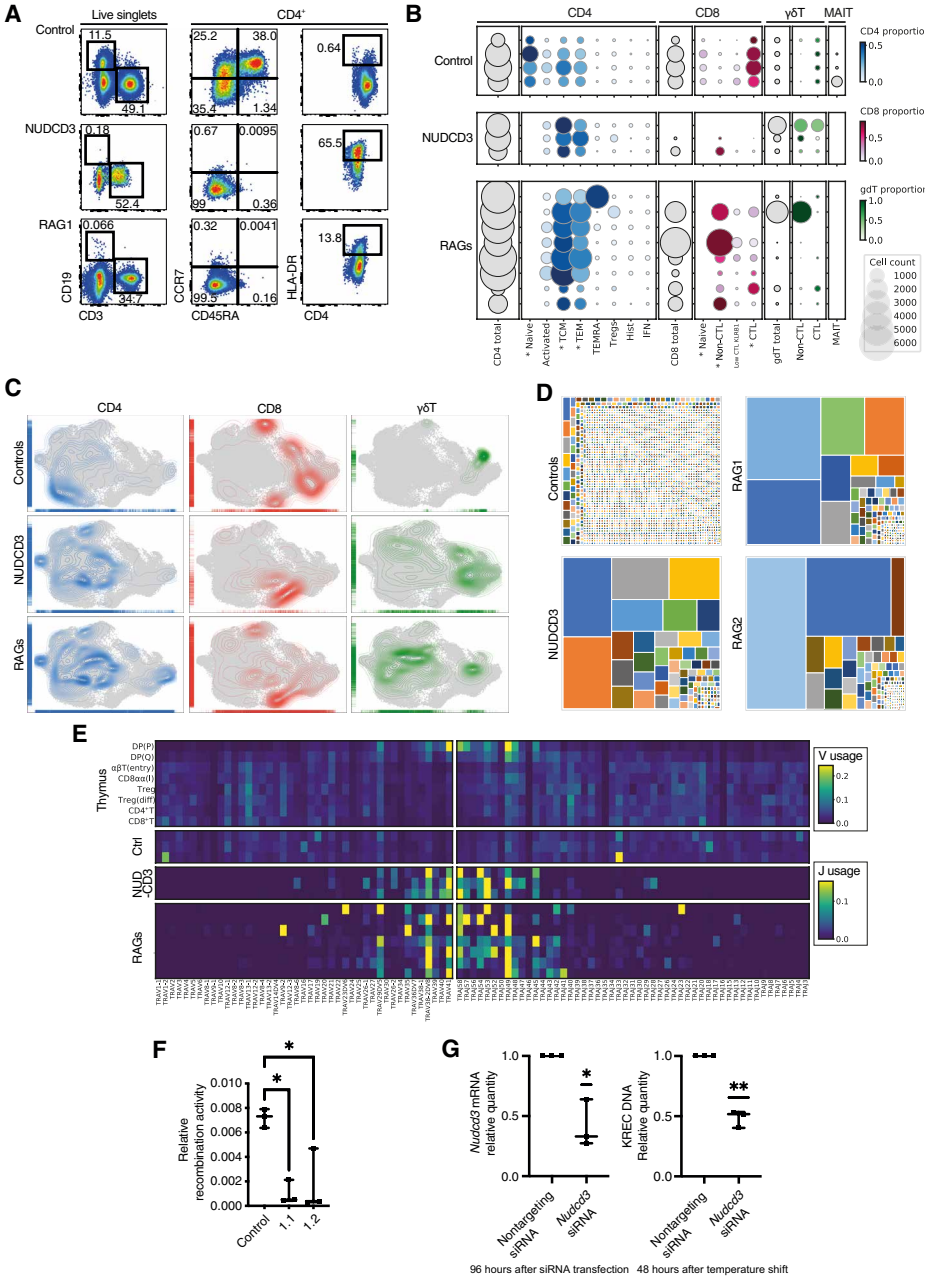

Fig. 2. Impaired V(D)J recombination underlies OS in infants with *NUDCD3*^{G52D}. (**A**) Representative flow cytometry plots showing a lack of B cells (CD19$^+$) and naïve CD4$^+$ T cells (CD45RA$^+$CCR7$^+$) and increase of activated CD4$^+$ T cells (HLA-DR$^+$) in representative patients with NUDCD3 and RAG1 OS compared with a healthy control. (**B**) Proportions of T cell subpopulations determined by scRNA-seq with dot size reflecting the number of cells and the color intensity corresponding to the proportion of all T cells per individual (one individual per row). Asterisks indicate a statistically significant difference in proportions for the comparison between healthy controls and patients with OS (patients with NUDCD3 and RAG grouped together) with FDR-corrected Mann-Whitney *U* test. (**C**) UMAP representation of CD4, CD8, and γδ T cells within T cell compartment across healthy individuals, as well as patients with OS with RAG or NUDCD3 variants. (**D**) T cell clonotype diversity in representative patients with OS and healthy control. Each tree map illustrates all unique clonotypes from one individual, each rectangle is one clonotype, and its size is proportional to the number of cells with this clonotype. Colors were chosen randomly to distinguish different clonotypes within a sample, and the same color does not represent shared clonotypes. Representative plots for a healthy individual and patients with OS with indicated underlying mutations. (**E**) *TRAV* and *TRAJ* gene usage distribution in patients with OS, healthy controls, and across the stages of human thymus development from (*24*). Each row corresponds to one individual. Genes are ordered according to their genomic position (left 5′ end to right 3′ end). **(F)** *NUDCD3*^{G52D} patient fibroblasts (1.1, 1.2) support reduced recombination of the substrate plasmid pDVG93 upon cotransfection with *RAG1* and *RAG2* compared with healthy control fibroblasts ($n = 3$) (levels of recombined pDVG93 expressed relative to total levels of transfected pDVG93). **(G)** Reduction in KREC production in mouse pre-B 103/BCL2 cells transfected with siRNA-targeting *Nudcd3* before a culture temperature shift from 33° to 39°C. DNA and RNA were harvested for qPCR, evaluating levels of *Nudcd3* mRNA transcripts relative to *Hprt1* (left) and levels of KREC relative to genomic *Alb* (right) ($n = 3$ independent experiments). In (F) and (G), data are shown as box and whisker plots, and comparison between groups was made by ANOVA/Bonferroni correction and one-sample *t* test, respectively. Statistical significance was defined as $*P < 0.05$ and $**P < 0.01$.

Downloaded from https://www.science.org at Leiden University on November 20, 2025

Given that these data indicated a conserved role for NUDCD3 in murine V(D)J recombination, we used CRISPR-Cas9 technology to engineer an in vivo mouse model bearing the homologous G52D missense variant on the C57BL/6 background (Fig. 3A). Mice homozygous for the *Nudcd3*^{G52D} variant (referred to below as *Nudcd3*^{Hom}) were born at sub-Mendelian frequency, were significantly smaller than littermates, and were sterile but appeared otherwise healthy (Fig. 3, B and C). Expression of NUDCD3 protein was substantially reduced in *Nudcd3*^{Hom} tissues compared with WT tissues (Fig. 3D and fig. S8A). Thymic cellularity was significantly lower than WT despite normal corticomedullary architecture (Fig. 3E and fig. S8B). We observed normal proportions of B and T cells in the periphery and a normal ratio of CD4 to CD8 T cells (Fig. 3, F to I, and figs. S8, C to F and S9, A and B). Nonetheless, the ratio of CD44^{hi} memory T cells to naïve T cells was consistently increased in the periphery of *Nudcd3*^{Hom} compared with WT littermates (fig. S8, G and H). Kappa light chain was overexpressed relative to λ light chain in peripheral B cells of *Nudcd3*^{Hom} mice, which would be expected in the context of impaired V(D)J recombination (Fig. 3, J and K, and fig. S9C) (*31*, *32*). Immunoglobulin production was preserved in *Nudcd3*^{Hom} mice, with slightly increased immunoglobulin M (IgM) and IgG2b and markedly increased IgE as is also seen in mice bearing *Rag1*$^{R972Q/R972Q}$ and *Rag2*$^{R229Q/R229Q}$ variants and in human patients with OS (Fig. 3L and fig. S9D) (*3*, *33*–*35*).

Developing thymocytes progress through an orderly series of stages as they undergo successive rounds of V(D)J recombination, express the resulting TCR, and traverse positive and negative selection checkpoints (*36*). To assess developmental progression, we analyzed the distribution of thymocytes by surface marker expression, noting a highly statistically significant excess of CD4^{-}CD8^{-} double-negative (DN) thymocytes in *Nudcd3*^{Hom} mice (Fig. 4, A and B, and fig. S10). Subdivision of the DN compartment showed that this expansion occurred at the DN3 (CD25^{hi}CD44^{lo}) stage (Fig. 4, A and C, and fig. S10, A to D), specifically the CD27^{lo} DN3a phase, which precedes pre-TCR signaling (Fig. 4, A and D) (*37*). Consistent with a developmental block, the absolute number of DN3a thymocytes in *Nudcd3*^{Hom} mice exceeded that in WT despite a much smaller thymus overall (Fig. 4D and Fig. 3E). Mutant mice also showed a relative expansion of the earliest DP subset (DP1), in which α chain rearrangement occurs (Fig. 4, A and E, and fig. S10, E to G). Although expanded, the CD25^{+} DN3 compartment proliferated less as assessed by Ki67 staining (fig. S10, H and I), whereas the frequency of Ki67^{+} cells within DP1 was not significantly reduced (fig. S10J). Subsequent development of CD4 and CD8 single-positive (SP) lymphocytes in *Nudcd3*^{Hom} mice appeared normal (fig. S11, A to G), although *Nudcd3*^{Hom} mice did exhibit a trend toward an increased proportion of thymic-derived regulatory T cells and markedly reduced invariant NK T (iNKT) cells, as previously described both in patients with *RAG*-OS and in a mouse model of this syndrome (fig. S11, H to K) (*34*, *38*). Thus, there is an incomplete block in *Nudcd3*^{Hom} thymocyte development at those stages where V(D)J recombination occurs. The expansion of these compartments (DN3a and DP1) implies a direct effect of *Nudcd3*^{Hom} on V(D)J recombination rather than a primary impairment of survival that shortens the time available for V(D)J recombination.

To explore this effect in greater detail, we isolated splenocytes and bulk-sequenced their rearranged TCR-encoding genes *Tra* and *Trb*. In comparison with WT, TCR clonotypes were less diverse in *Nudcd3*^{Hom} mice, and individual clonotypes tended to be more expanded (Fig. 4F and fig. S12, A and B) out of proportion to the lower fraction of naïve cells. Echoing human *NUDCD3*^{G52D} patients, *Nudcd3*^{Hom} mice showed strongly skewed *Tra* gene usage toward V segments from the 3′ end of the V locus and J segments from the 5′ end of the J locus and the absence of a similar effect for *Trb* or *Ig* gene segments (Fig. 4G and fig. S12, E to H) (*26*). This skewing likely explained the lack of iNKT cells (figs. S11, J and K and fig. S12C), which strongly favor the use of distal *Tra* segments (*39*). In addition, *Nudcd3*^{Hom} mice had fewer nonproductive *Trb* chain rearrangements than WT (fig. S12D). These exist only if an unproductive recombination is followed by a successful second round of recombination, ensuring T cell survival. Thus, both the pattern of TCR gene segment usage and the lack of nonproductive rearrangements suggest a lower frequency of repeated recombinations of *Tra/Trb* loci in *Nudcd3*^{Hom} mice as in humans.

In parallel, we analyzed B cell development through enumeration of successive Hardy fractions in mouse BM by flow cytometry (fig. S13A). There was a relative accumulation of IgM^{-}IgD^{-} (fraction D) pre-B cells and a trend toward a reduction in mature IgM^{+}IgD^{+} B cells (fraction F) but no effect on pro-B cell populations (fractions A to C) (fig. S13, A to D). Thus, both T and B cell development are perturbed in *Nudcd3*^{G52D} mice, although to a lesser degree than that observed in human *NUDCD3*^{G52D} patients or in published mouse models of hypomorphic RAG deficiency, especially in the case of B cells (*33*–*35*).

To examine whether this alteration of lymphocyte development was cell intrinsic, we prepared mixed BM chimeras and compared the ability of *Nudcd3*^{Hom} and *Nudcd3*^{WT} cells to contribute to the B and T cell compartments of a WT host. Lethally irradiated mT^{+}CD45.1^{+} WT recipient mice were injected intravenously with equal amounts of CD45.1^{+} WT and CD45.2^{+} *Nudcd3*^{Hom} or *Nudcd3*^{WT} whole BM cells (fig. S13, E and F). *Nudcd3*^{Hom} cells failed to develop normally when in competition with WT cells, as demonstrated by their underrepresentation throughout T cell development (Fig. 4H). The reduction at DN1 implied that *Nudcd3*^{Hom} had a possible background effect on early thymocyte fitness relative to WT, which was not strong enough, however, to prevent the relative expansion of the subsequent (DN2 to DN3a) stages. However, further marked skewing of the DN3b compartment toward WT cells (Fig. 4H) indicated defective developmental transition of *Nudcd3*^{Hom} thymocytes from DN3a to DN3b, confirming the impaired DN3a to DN3b progression observed in steady-state *Nudcd3*^{Hom} mice. This skewing was exacerbated at the transition to the DP stage, again echoing the phenotype seen in the steady-state *Nudcd3*^{Hom} model. By contrast, the contribution of *Nudcd3*^{Hom} cells to the developing B cell compartment appeared consistent throughout development until a reduction in mature IgM^{+}IgD^{+} B cells (fraction F) (fig. S13G). Nonetheless, the percentage of Igλ^{+}CD45.2^{+} *Nudcd3*^{Hom} cells was very low (fig. S13H), consistent with defective light chain rearrangement despite the normal proportion of *Nudcd3*^{Hom} cells in fractions D and E.

Although we do not formally exclude an additional contribution from altered thymic function, the mixed BM chimera experiments confirm the cell-intrinsic nature of both B and T cell abnormalities in the *Nudcd3*^{Hom} mouse. This is in keeping with the curative potential of HSCT demonstrated in two of the infants in our case series, who both achieved long-term B and T cell reconstitution with independence of immunoglobulin replacement therapy (table S2). Thus, *NUDCD3*^{G52D} appears to produce an incomplete developmental

Downloaded from https://www.science.org at Leiden University on November 20, 2025

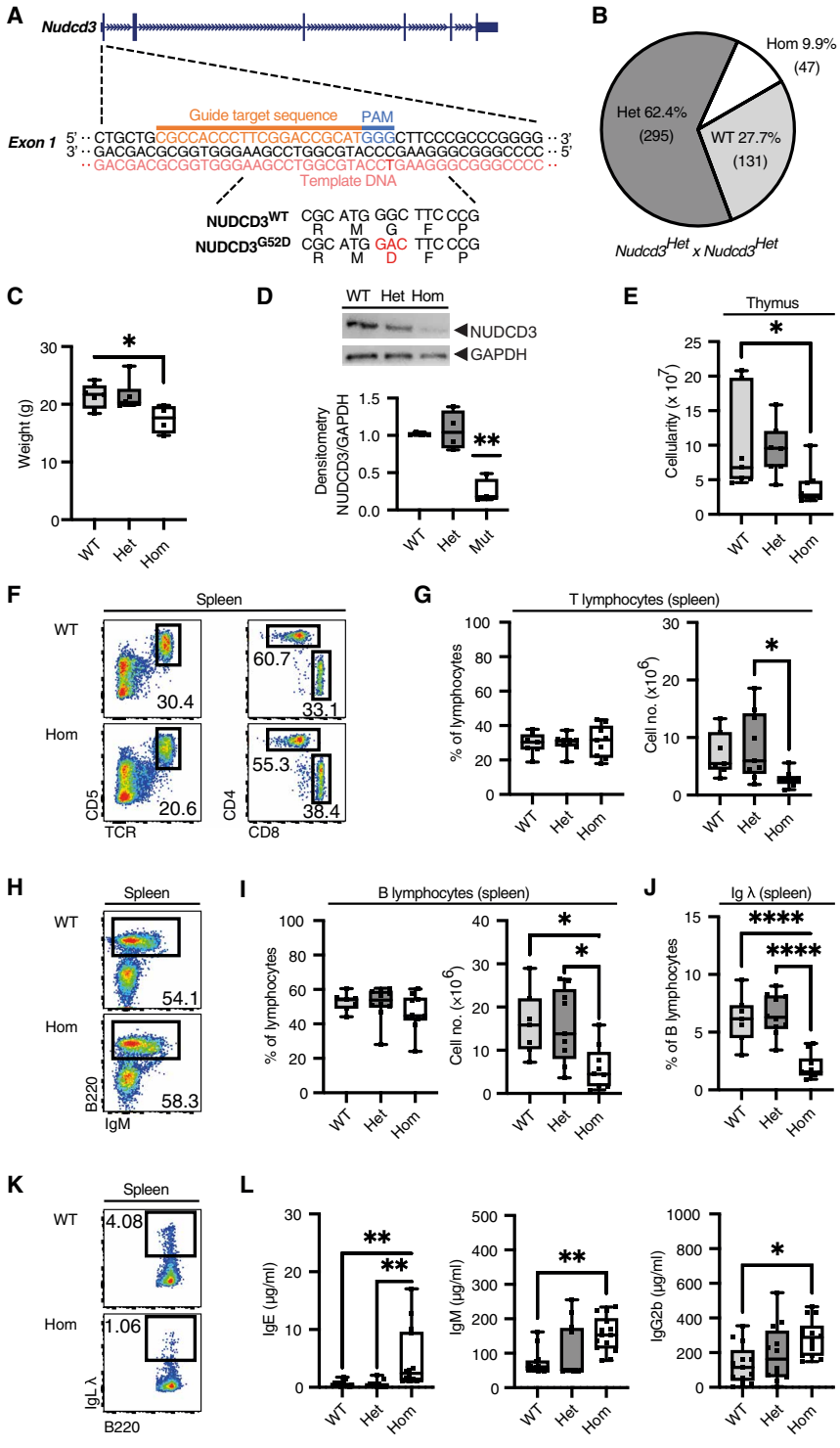

Fig. 3. Generation of a knock-in mouse model of NUDCD3^{G52D}. (**A**) CRISPR-Cas9 guide target sequence introducing the missense mutation c.155G>A (p.G52D) to mouse *Nudcd3*. (**B**) Reduced Mendelian ratios of mice born to 19 *Nudcd3*^{Het} breeding pairs ($n = 473$ pups). (**C**) *Nudcd3*^{Hom} mice ($n = 5$) are smaller than *Nudcd3*^{WT} ($n = 8$) and *Nudcd3*^{Het} ($n = 7$) littermate controls, aged 5 to 8 weeks. (**D**) Immunoblotting shows reduced expression of NUDCD3 protein in splenocytes from *Nudcd3*^{Hom} ($n = 4$) mice compared with littermate controls ($n = 4$) using a GAPDH loading control. (**E**) Thymic cellularity is reduced in *Nudcd3*^{Hom} ($n = 8$) mice compared with littermate controls (WT $n = 6$ and Het $n = 8$) aged 5 to 14 weeks. **(F)** Comparable frequency of splenic T lymphocytes (CD5^{hi}TCR^{hi}) within forward/side scatter (FSC/SSC) lymphocyte gate (left) and CD4 and CD8 T lymphocytes (of T lymphocytes) (right), T lymphocytes quantified in (**G**) between genotypes (WT, $n = 7$; Het, $n = 10$; Hom, $n = 10$). **(H)** Comparable frequency, within FSC/SSC lymphocyte gate, of splenic B lymphocytes (B220^{hi}IgM^{hi}), quantified in (**I**) between genotypes. (**J**) Reduced frequency of lambda light chain expressing B lymphocytes (IgLλ^{hi}) in the spleens of *Nudcd3*^{Hom} mice compared with *WT* and *Het* littermates. (**K**) B cell λ light chain usage (IgLλ^{hi}). (**L**) Increased IgE (left), IgM (middle), and IgG2 (right) in serum from *Nudcd3*^{Hom} mice compared with that of *Nudcd3*^{WT} and *Nudcd3*^{Het} littermates ($n = 7$). Data, pooled from multiple experiments (see data S3), are shown as box and whisker plots with *Nudcd3*^{WT} (light gray), *Nudcd3*^{Het} (dark gray), and *Nudcd3*^{Hom} (white). Comparisons between groups were made by ANOVA/Bonferroni except in (D), where one-sample *t* test was applied. Statistical significance was defined as $^{*}P < 0.05$, $^{**}P < 0.01$, and $^{****}P < 0.0001$.

block with its major impact on V(D)J recombination in both species, one that differs in severity between humans and mice and between developing B and T cells.

Failure of RAG2-dependent disaggregation of RAG1 in NUDCD3-deficient cells

To further investigate this impact on V(D)J recombination, we next harvested *Nudcd3*^{WT}, *Nudcd3*^{Het}, or *Nudcd3*^{Hom} mouse BM and generated pre-B cell lines containing an inverted green fluorescent protein (GFP) recombination reporter (Fig. 5A). Upon triggering by v-Abl inhibition, WT pre-B cells successfully recombined the reporter construct to generate green fluorescence. By contrast, *Nudcd3*^{Hom} pre-B cells showed markedly reduced recombination activity (Fig. 5A). Thus, a primary defect in V(D)J recombination appears to arise from the *Nudcd3* p.G52D mutation rather than an indirect effect through impaired cell survival.

To gain insight into the molecular mechanism of this defect, we first considered the possibility that the G52D variant might disrupt a normal interaction between NUDCD3 and RAG1 and/or RAG2 such as a cochaperone function required for stabilization and/or localization. By immunofluorescence microscopy, we found no evidence of altered subcellular distribution of either RAG protein when overexpressed alone in mutant versus WT cells, suggesting that the nuclear import of folded RAGs was intact (Fig. 5B). We did, however, note that the distribution of NUDCD3 was altered by RAG expression in 293T cells, becoming increasingly nuclear (fig. S14A). Despite this, neither coimmunoprecipitation followed by immunoblotting nor mass spectrometric (MS) analysis showed a direct interaction between NUDCD3 and endogenous RAGs in a RAG-expressing T lymphoblastoid cell line, although we confirmed other previously reported protein-protein interactions

Downloaded from https://www.science.org at Leiden University on November 20, 2025

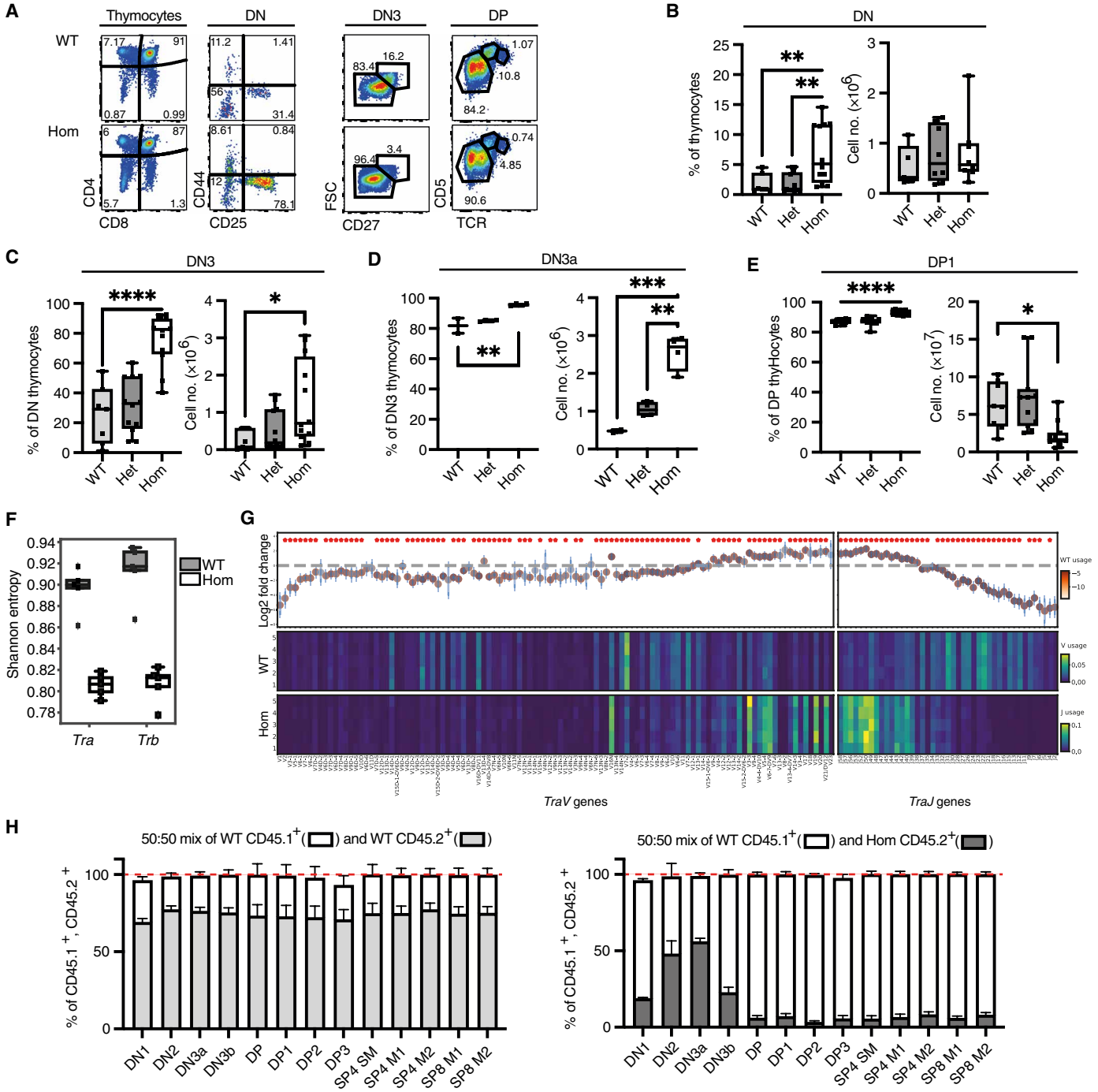

Fig. 4. Impaired V(D)J recombination in *NUDCD3*^{Hom} mice. (**A**) Accumulation of DN (CD4$^-$CD8$^-$), DN3 (CD44$^-$CD25$^+$), DN3a (CD27lo), and DP1 (CD5^{lo}TCR^{hi}) thymocytes in *Nudcd3*^{Hom} mice compared with littermate controls. Increased frequency (left) of DN (**B**), DN3 (**C**), DN3a (**D**), and DP1 (**E**) thymocytes with corresponding enumeration (right) [gating is as per fig. S10A; WT, $n = 7$; Het, $n = 12$; Hom, $n = 12$ except for (D), where WT, $n = 2$; Het, $n = 4$; Hom, $n = 4$]. In (B) to (E), data are shown as box and whisker plots with *Nudcd3*^{WT} (light gray), *Nudcd3*^{Het} (dark gray), and *Nudcd3*^{Hom} (clear). Comparisons between groups were made by ANOVA/Bonferroni, and statistical significance was defined as $^*P < 0.05$, $^{**}P < 0.01$, and $^{****}P < 0.0001$. (**F**) Diversity of TCRα and TCRβ (as Shannon entropy) in WT and *Nudcd3*^{Hom} mice (FDR-corrected $P < 0.01$, Mann-Whitney *U* test). (**G**) *TraV* and *TraJ* usage in WT and *Nudcd3*^{Hom} mice. Bottom panel organized as in Fig. 2E, and the top panel shows $\log_2$ fold change between *Nudcd3*^{Hom} and WT mice. Asterisk indicates a statistically significant difference with FDR-corrected $P < 0.01$, Mann-Whitney *U* test. (**H**) Proportion of thymocyte subsets in lethally irradiated mice reconstituted for 28 days with equal mixtures of *Nudcd3*^{WT} ($n = 7$) or *Nudcd3*^{Hom} ($n = 6$) CD45.2$^+$ and WT CD45.1$^+$ BM. Bars (mean with SE of the mean) shown with CD45.2$^+$ (filled) and CD45.1$^+$ (white).

Downloaded from https://www.science.org at Leiden University on November 20, 2025

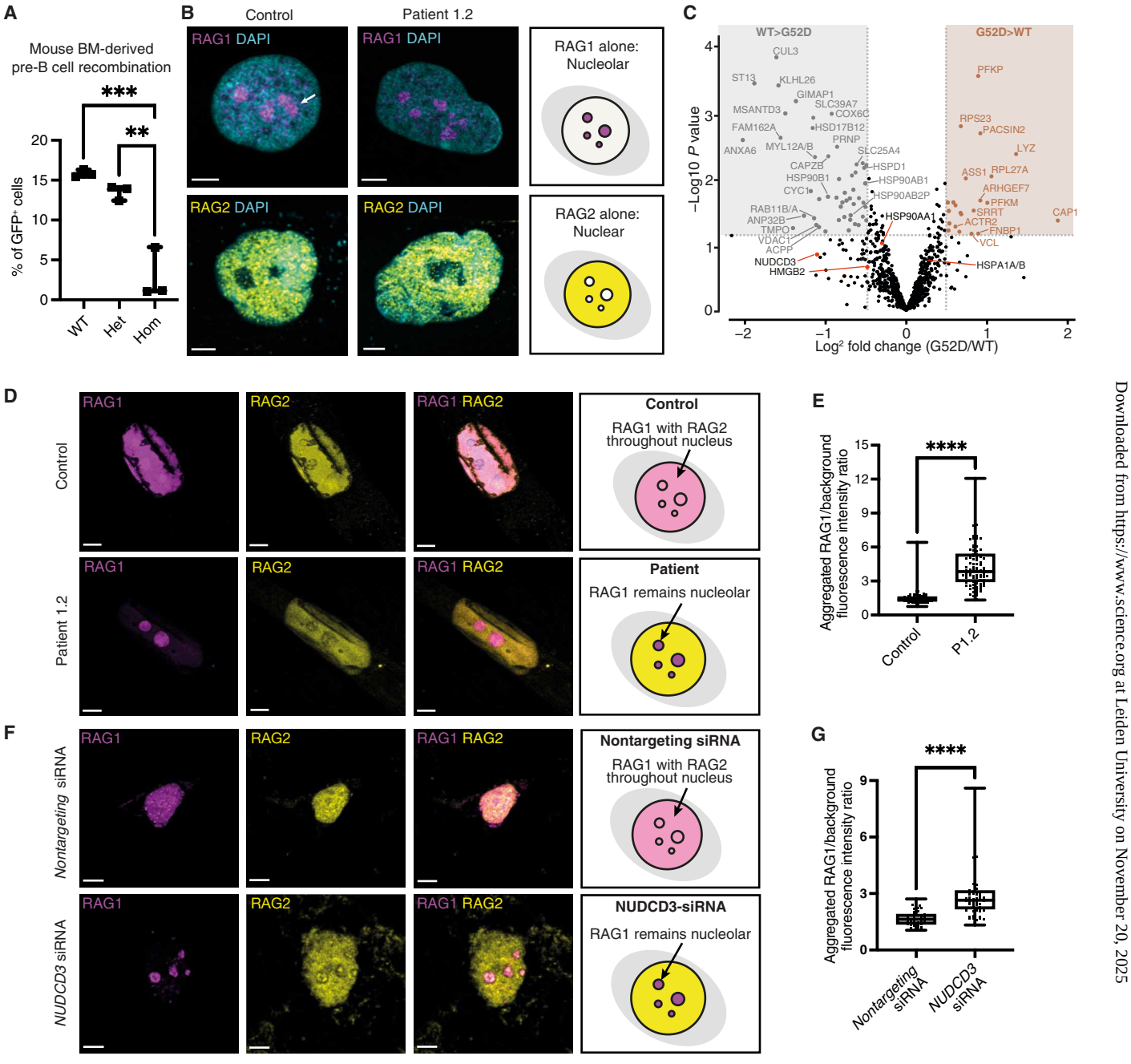

Fig. 5. Sequestration of RAG1 in nucleoli of NUDCD3-deficient cells. (**A**) In vitro recombination reporter assay in pre-B cell lines generated from *Nudcd3*^{WT}, *Nudcd3*^{Het}, and *Nudcd3*^{Hom} mice. GFP positivity was used as a marker of RAG-dependent recombination (right) ($n = 3$ experiments), and comparisons between groups were made by ANOVA/Bonferroni. (**B**) Normal intranuclear distribution of V5-tagged RAG1 (magenta) and RAG2 (yellow) was individually expressed in patient fibroblasts, was imaged by confocal microscopy with counterstain nuclear marker DAPI (cyan) (scale bars, 5 μm), and is represented in schematic (below). (**C**) Volcano plot comparing differentially interacting proteins between WT and G52D NUDCD3, ascertained by mass spectrometry with significance cutoffs indicated at $\log_2$ fold change ≥ 0.5 and $P < 0.05$ ($-\log_{10} P > 1.3$). (**D**) Aberrant nucleolar localization of RAG1 in patient fibroblasts cotransduced with *RAG1* and *RAG2*. Representative confocal microscopy images pseudocolored for RAG1 (magenta) and RAG2 (yellow) (scale bars, 5 μm) with schematic representation of data. (**E**) Quantification of RAG1 signal intensity in nucleoli compared with the rest of the nucleus, shown in box and whisker plots ($n = 65$ control and $n = 99$ NUDCD3^{G52D} (P1.2) *RAG1*/*RAG2*-cotransduced fibroblasts analyzed). (**F**) Impaired RAG2-dependent redistribution of RAG1 from nucleoli of *NUDCD3*-knockdown HEK293T cells. Representative confocal microscopy images colored as in (D) (scale bars, 5 μm) with schematic representation of data. (**G**) Quantification of nucleolar signal intensity relative to rest of nucleus as in (E) ($n = 43$ nontargeting control and $n = 61$ *NUDCD3* knockdown cells analyzed). Further images for (D) and (F) are in fig. S14 (B and D). Comparison between groups was made by ANOVA/Bonferroni in (A) and unpaired *t* test in (E) and (G), and statistical significance was defined as $^{**}P < 0.01$, $^{***}P < 0.001$, and $^{****}P < 0.0001$.

Downloaded from https://www.science.org at Leiden University on November 20, 2025

(Fig. 5C, table S6, and data S1) (*18*, *40*). The interactomes of WT and G52D NUDCD3 were largely overlapping and included several previously identified binding partners of RAGs such as heat shock proteins, leaving open the possibility of an indirect interaction.

Immunofluorescence imaging demonstrated the previously described reciprocal nuclear localization of individually expressed RAG proteins, either inside (RAG1) or outside (RAG2) nucleoli (Fig. 5B) (*41*). Recent reports have emphasized that the nucleolar retention of RAG1 restrains RAG recombinase activity (*40*) and that cell cycle–dependent RAG2 coexpression enables the redistribution of its partner from nucleoli (*42*). We therefore investigated the impact of *NUDCD3*^{G52D} upon RAG2-dependent RAG1 redistribution by cotransducing primary fibroblasts with fluorescently tagged RAG1 and RAG2. Control fibroblasts showed partial colocalization of RAG proteins outside nucleoli, whereas RAG1 was predominantly confined to the nucleoli of dual-transduced patient fibroblasts (Fig. 5, D and E, and fig. S14, B and C). We confirmed that the nucleolar egress of RAG1 was truly NUDCD3 dependent by performing a similar experiment in HEK293T cells in which *NUDCD3* had been partially knocked down by siRNA transfection before transient overexpression of the fluorescently tagged RAGs (Fig. 5, F and G, and fig. S14, D and E). The mislocalization of RAG1 in *NUDCD3*-deficient *RAG2*-cotransfected cells was accompanied by an overall increase in RAG1 protein expression as assessed by immunoblotting (fig. S15A). We were unable to examine the subnuclear localization of endogenous RAGs in a more physiological context because appropriate antibodies for fluorescence microscopy are currently unavailable. However, immunoblotting of *Nudcd3*^{Hom} thymic lysates revealed the overexpression of RAG1 in keeping with its nucleolar accumulation in the absence of WT NUDCD3 (fig. S15B). Thus, the redistribution of RAG1 from nucleoli, known to be necessary for its recombinase function, not only is RAG2 dependent but also requires a specific activity of NUDCD3 that the G52D allele lacks.

DISCUSSION

These studies establish *NUDCD3* as a disease gene for T-B- SCID and OS. Its integrity is required for efficient B and T cell development, specifically for RAG-dependent V(D)J recombination, and consequently the generation of antigen receptor diversity upon which adaptive immunity depends. The close phenocopy between human *NUDCD3*^{G52D}- and *RAG*-related OS suggests that these disorders would behave similarly in response to treatment. Two of the eight *NUDCD3*-mutated patients who progressed to HSCT survived, whereas the remaining patients succumbed to a variety of infectious and inflammatory complications (table S1). The generally poor outcome of this cohort highlights the life-threatening nature of SCID/OS and the importance of early diagnosis and therapy. Infants with suspected T cell immunodeficiency, including those identified through newborn T cell receptor excision circle (TREC) screening, should be tested for pathogenic variants of the *NUDCD3* gene.

The focus of this work was to understand the role of NUDCD3 within the immune system because of the severity of the G52D-associated immunological phenotype, the absence of consistent extraimmune features, and the long-term survival of two affected individuals after HSCT. However, given its widespread expression and behavior in essentiality screens, it is likely that human NUDCD3 performs other functions that are less sensitive to the G52D substitution and/or overall NUDCD3 expression level. That knock-in mice were small and sterile may well reflect the compromise of certain core functions of murine NUDCD3, perhaps in keeping with the mouse homolog's lower protein expression. It is expected that there would be differences in the degree of redundancy and sensitivity to individual missense mutations between mouse and human homologs. Further work will be required to clarify the NUDCD3 interactome and the extent to which NUDCD3's functions can be fulfilled by alternative cochaperones among different cell types and species.

The molecular mechanism by which RAG2 enables the egress of RAG1 from nucleoli has so far been elusive. First described as a hub for ribosome biogenesis, nucleoli have been proposed to play an important part in nuclear protein quality control based on the nucleolar colocalization of metastable nuclear proteins with chaperones such as Hsp70 after heat stress that can enable their refolding (*43*, *44*). The observed nucleolar retention of RAG1 may therefore reflect its tendency toward aggregation and its possession of a specific arginine- and histidine-rich motif previously determined to be a nucleolar retention signal (*40*). Nonetheless, a regulatory aspect to this arrangement is implied by the observations that forced nucleolar exclusion of RAG1 favors increased recombination activity (*40*) and that decoupling RAG2 expression from the cell cycle leads to genomic instability and lymphoid tumorigenesis (*8*). A parsimonious model would see NUDCD3 cooperating with RAG2 and heat shock proteins to enable RAG1 to refold and exit the nucleolus, a cochaperone function reminiscent of that executed by other NudC family members with respect to distinct client proteins (*19*, *20*). NUDCD3^{G52D}, possibly because of its impaired homodimerization, is unable to fulfil this cochaperone function efficiently, leading to the insufficient withdrawal of RAG1 from nucleoli and diminished recombinase activity. The milder impact of this variant in mice, especially on the B cell compartment, implies greater redundancy with respect to this key immunological function, possibly supported by alternative cochaperones. Understanding this complex biology promises additional perspectives on V(D)J recombination and related disorders.

MATERIALS AND METHODS

Human participants

Patients were cared for by Newcastle upon Tyne Hospitals NHS Foundation Trust or Oslo University Hospitals. Written informed consent was provided by all human participants or their legal guardians in accordance with the 1975 Helsinki principles for enrollment in research protocols that were approved by the Newcastle and North Tyneside Research Ethics Committee 1, UK (REC reference 16/NE/0002) or by the regional ethical committee for medical and health research ethics in Norway (REC South East).

Genetic analysis

DNA was obtained from patient peripheral blood mononuclear cells or dermal fibroblast cultures using QIAGEN's DNeasy Kit. After library preparation and target enrichment using the Agilent SureSelect Human All Exon Kit (version 2 or 5), WES was performed on an Illumina platform. Alignment, variant calling, and annotation were performed by standard methods based on Genome Analysis Toolkit best practice and ANNOVAR (Annotate Variation). Pathogenic variants in known disease-causing genes were first excluded by querying against a virtual panel based on the contemporary IUIS

Downloaded from https://www.science.org at Leiden University on November 20, 2025

(International Union of Immunological Societies) classification (*2*). Exome data from family 1 (individuals 1.1 and 1.2) were cross-referenced with family 2 (proband 2.1) to identify shared rare homozygous nonsynonymous variants, of which *NUDCD3* c.155G>A was the sole instance. Exome data from patient 3.1 were obtained separately but revealed the same homozygous variant. Variant genotypes of cases and their family members were confirmed by Sanger sequencing (Fig. 1, A and B) using the following sequencing primers: forward: 5′-GGCAACGTCCAGGATTTCC-3′; reverse: 5′-TCCTCCTTTTCCTGGTGTCC-3′.

Plasmid construction

NUDCD3 was cloned into pDONR207, pCR3-C-HA, and pCR3-C-Myc by Gateway cloning. Site-directed mutagenesis on pDONR207-NUDCD3 to generate G155A variant was performed by the Agilent QuikChange II XL Kit according to the manufacturer's instruction using the following primers: forward: 5′-CGGGCGGGAAGTCCATGCGGTCC-3′ and reverse: 5′-GGACCGCATGGACTTCCCGCCCG-3′. HA-tagged WT/G155A mutant NUDCD3 was cloned into pCDH-EF1α-MCS*-T2A-GFP for mass spectrometry purposes using pDONR221-NUDCD3-2×HA purchased from Invitrogen GeneArt Gene Synthesis as templates. *RAG1*- or *RAG2*-containing pDONR223 plasmids were purchased from Horizon Discovery. Depending on the purposes of either transient transfection or lentiviral transduction, relevant coding sequences were subcloned into pLenti6/V5-DEST (Invitrogen), pDEST-N-eGFP (Addgene), pDEST-N-mCherry (Addgene) by Gateway LR reaction. Lentiviral transfer plasmids pLenti-RAG1-eGFP and pLenti-RAG2-mCherry were created by substituting V5-tag in pLenti6-RAG1/RAG2-V5 with enhanced GFP (eGFP) and mCherry CDS cloned from pDEST-N-eGFP and pDEST-N-mCherry using Bst BI and Age I restriction sites. The primers for cloning eGFP and mCherry CDS were: forward: 5′-GGGCCCGCGGTTCGAAATGGTGAGCAAGGGCGAG-3′ and reverse: 5′-TACTAACCGGTACGTTACTTGTACAGCTCGTCC-3′. Retroviral transfer plasmids pMSCV-v-Abl and pMGINV were provided by B.-R. Chen and B. Sleckman (University of Alabama, Birmingham). *Bcl2* retroviral plasmid was created by replacing the expression cassette in TCR OTI-2A.pMIG II (Addgene, #52111) with murine *Bcl2* CDS (NM_009741.5) using Bgl II and Not I restriction sites.

Immunoblotting

Relevant cells were washed with phosphate-buffered saline (PBS) and lysed using radioimmunoprecipitation assay buffer [150 mM sodium chloride, 1% Triton X-100, 0.5% sodium deoxycholate, 0.1% SDS, and 50 mM tris (pH7.4)] supplemented with cOmplete Protease Inhibitor Cocktail and PhosSTOP Phosphatase inhibitor Cocktail (Roche, Switzerland). Lysates were centrifuged at 14,000*g* for 10 min, and cleared supernatants were denatured at 70°C for 15 min with 10% dithiothreitol (DTT) and 1X NuPAGE lithium dodecyl sulfate (LDS) Sample Buffer (Thermo Fisher Scientific, USA). Samples were then loaded on to 4 to 12% bis-tris gel alongside prestained protein ladder (PageRuler Plus, Thermo Fisher Scientific, USA) for gel electrophoresis in 1X NuPAGE MOPS SDS Running Buffer (Invitrogen, USA). Either an equal volume of lysate was loaded or the protein concentration was measured with the bicinchoninic acid (BCA) protein assay (Thermo Fisher Scientific, USA) before loading. Proteins were transferred to 0.45-μm polyvinyl difluoride membranes (Millipore, USA) at 20 V using 1X NuPAGE Transfer Buffer (Invitrogen, USA) in 20% methanol. Membranes were blocked for 60 min using either 5% bovine serum albumin in tris-buffered saline with 0.1% Tween 20 or 5% milk before immunostaining. Membranes were incubated overnight with relevant primary antibodies, followed by the appropriate secondary antibody. Membranes were developed with Immobilon ECL substrate (Millipore, USA), and chemiluminescent images were visualized with the LI-COR Odyssey (LI-COR, USA) with LI-COR Image Studio software version 5.2.5. Primary and secondary antibodies used for immunoblotting and their normal dilutions are listed in data S2.

Size exclusion chromatography

HEK293T cells were seeded in 100-mm-diameter petri dishes at 4×10^6 cells per plate, followed by polyethylenimine (PEI; Sigma-Aldrich) transfection with 8 μg of WT or G52D mutant NUDCD3 plasmids (both in pEBB backbone). Transfected cells were lysed in a lysis buffer with 50 mM Hepes-KOH, 150 mM or 500 mM NaCl, 2 mM EDTA, 5% glycerol, and 0.5% Triton X-100 (pH 7.5). Lysates were then applied to a Superose 12 column (GE Healthcare) and eluted in PBS at a rate of 0.5 ml/min. Fractions were precipitated with trichloroacetic acid using recombinant human insulin (Sigma-Aldrich) as a carrier, and pellets were resuspended in 100 μl of 1X LDS sample buffer (Thermo Fisher) with 1 mM DTT. Samples were then heated and analyzed by immunoblotting as described above.

Coimmunoprecipitation

Cells were lysed in immunoprecipitation (IP) buffer composed of 25 mM tris (pH 7.4), 1 mM EDTA, 150 mM NaCl, 1% NP-40, 1 mM sodium orthovanadate, and 10 mM sodium fluoride with Roche cOmplete proteinase inhibitor. The cell lysates were centrifuged at 17,000*g* at 4°C for 10 min. Soluble fractions were precleared for 1 hour at 4°C with Protein G Sepharose 4 beads (Fast Flow, GE Healthcare) that were blocked with 1% bovine serum albumin (BSA) IP buffer for 1 hour. Precleared cell lysates were immunoprecipitated overnight with blocked beads that were incubated with antibody for 1 hour. Protein G Sepharose beads were washed three times in IP buffer and then boiled with 4X LDS buffer at 95°C for 10 min to elute the absorbed immunocomplexes. Pulldown samples were analyzed by immunoblotting as described above. IP for mass spectrometry is described below.

Lentiviral and retroviral transduction

Lentiviruses were produced using Invitrogen ViraPower Lentiviral Systems (Thermo Fisher Scientific) or by cotransfection of psPAX2, pCMV-VSV-G (provided by D. Young) and the relevant lentiviral transfer plasmid into HEK293T cells using PEI. Viral particle–contained supernatant was collected 48 to 96 hours after transfection and filtered with a 0.45-μm sterile filter. Viral particles were purified by mixing the supernatant with Lenti-X Concentrator (TaKaRa 631231) according to the manufacturer's instruction, and the mixture was centrifuged at 1500*g* at 4°C for 45 min before the pellet was resuspended in 1% of the original volume of supernatant. Patient or healthy donor dermal fibroblasts or MOLT4 cells were spinoculated in six-well plates for 1.5 hours at 845*g*, with target or null control viral particles serially diluted in a total volume of 0.5 ml of Dulbecco's modified Eagle's medium (DMEM)/RPMI containing hexadimethrine bromide (8 mg/ml) (Polybrene, Sigma-Aldrich). Cells were rested in virus-containing medium for 8 hours and then incubated in fresh DMEM/RPMI for 48 hours, when they were selected in

Downloaded from https://www.science.org at Leiden University on November 20, 2025

DMEM containing blasticidin (4 mg/ml) (Thermo Fisher Scientific), or transduced MOLT4 cells were sorted according to GFP intensity. Blasticidin-containing medium was refreshed every 72 hours.

Retroviruses were produced by cotransfecting HEK293T cells with pCL-Eco (Addgene, #12371) and relevant retroviral transfer plasmid using PEI. Viral particle–containing supernatant was collected 48 hours after transfection and filtered with a 0.45-μm sterile filter. Viral particles were purified by centrifuging at 16,639*g* for 4 to 5 hours at 4°C. Mouse mononuclear BM cells were isolated from BM harvested from femus and tibia by Histopaque 1083 using the manufacturer's instructions. These mononuclear BM cells were cultured in BM medium [RPMI supplemented with 15% fetal bovine serum, 5 μM 2-mercaptoethanol (Sigma-Aldrich), 2 mM L-glutamine, penicillin (100 U/ml), and streptomycin (0.1 mg/ml; Sigma-Aldrich)]. A total of 5×10^5 mononuclear BM cells were spinoculated in 48-well plates for 75 min at 1600*g* with viral particles diluted in a total volume of 0.2 ml of BM medium containing Synperonic F 108 (1 mg/ml; Sigma-Aldrich) and murine IL-7 (10 ng/ml; BioLegend). Transduced cells were cultured in 1 ml of BM medium that was refreshed every 48 to 72 hours.

Coimmunoprecipitation mass spectrometry (CoIP/MS)

A total of 2×10^8 MOLT4 cells transduced with empty vector, hemagglutinin (HA)–tagged WT, or G52D NUDCD3 were lysed in 1% NP-40 buffer by sonication. PureProteome Protein A/G Mix magnetic beads were crosslinked with 20 μg of anti-HA antibody (Abcam, ab9110) using 25 mM dimethyl pimelimidate (Thermo Fisher Scientific) in 200 mM triethanolamine buffer (Sigma-Aldrich) and quenched with addition of tris (pH 7.4). The immunoprecipitation was performed by loading precleared lysate to conjugated beads at 4°C overnight before washing and elution with 2.5% SDS in 100 mM AmBic three times. Samples were digested into peptides by ProtiFi S-Trap Micro Spin Column kit according to the manufacturer's recommended protocol. Proteins were reduced with 20 mM tris(2-carboxyethyl)phosphine hydrochloride (Sigma-Aldrich) at 37°C for 30 min and alkylated with 20 mM iodoacetamide (Sigma-Aldrich) in the dark for 30 min. A ratio of 1:10 (w:w) TPCK-treated trypsin (Worthington-Biochem) was used to digest the samples for 2 hours at 47°C. Eluted peptides were dried down and resuspended in 5% formic acid. Peptides were analyzed by nanoflow LC-MS/MS using a Fusion Lumos Tribrid Orbitrap mass spectrometer (Thermo Fisher Scientific) coupled to a Dionex UltiMate 3000 with an active gradient of 60 min, following the conditions published previously (*45*).

All discovery proteomics RAW mass spectra were analyzed using MaxQuant (version 1.6.5.0) (*46*) and searched against a SwissProt *Homo sapiens* database (*47*, *48*) as previously described (*45*). The statistical analysis was done using the R package Limma with a Benjamini-Hochberg false discovery rate (FDR) threshold of P value of <0.05 (*49*).

Immunofluorescence and microscopy

Fibroblasts transduced with lentiviruses encoding V5- or eGFP- or mCherry-tagged RAG1 or RAG2, HeLa cells transfected with plasmids encoding HA- or Myc-tagged WT/G52D NUDCD3, or HEK293T cells transfected with nontargeting siRNA/*NUDCD3* siRNA (Thermo Fisher Scientific, Silencer Select s23709, s23711, 4390843) using DharmaFECT 1 (Horizon) followed by plasmids encoding eGFP-tagged RAG1 and mCherry-tagged RAG2 in μ-Slide eight-well ibiTreat chamber slide (ibidi, Germany) were fixed with 4% formaldehyde for 15 min and washed with PBS. Slides were blocked with 10% goat serum and permeabilized with 0.1% Triton X-100 in PBS and then incubated with relevant antibodies at 4°C overnight. Slides were then washed with 0.1% Tween 20 in PBS and incubated with appropriate secondary antibodies for 1 hour at room temperature, followed by nuclear staining with 4′,6-diamidino-2-phenylindole (DAPI) (0.2 μg/ml; Thermo Fisher Scientific, USA). Slides were mounted with ProLong Glass Antifade Mountant (Thermo Fisher Scentific, USA) and imaged on a Leica SP8-STED confocal microscope with a Leica HC PL APO 63×/f1.40 oil CS2 lens. The image acquisition was carried out by Leica LAS X software (version 3.3.0.16799). Confocal images were deconvolved and analyzed by Huygens Essential/Professional software (version 23.04). For the analysis of nucleolar localization, Leica LAS X software was used to measure average raw fluorescence intensity of region of interest using Line Profile and Stack Profile tools, and results are presented as a simple ratio. The primary and secondary antibodies used are listed in data S2.

Mouse tissues fixed in 4% formaldehyde in PBS were paraffin-embedded and sectioned at 8 μm and hematoxylin and eosin–stained by the Laboratories of the Integrated Laboratory Medicine Directorate, Newcastle upon Tyne Hospitals NHS Foundation Trust. Slides were imaged using an Olympus BX43 with an Olympus PLN Plan Achromat 10×/f0.25 lens, SC50 camera, and cellSens Standard software (version 1.16, build 15404 software).

Reverse transcription quantitative PCR

RNA was extracted by lysing cells in TRIzol reagent (Thermo Fisher Scientific). Chloroform was added to 1/5 total sample volume, and the sample was centrifuged for 15 min at 12,000 *g* at 4°C. The top aqueous phase was transferred to a new tube, and 2.5 V of aqueous phase of 75% ethanol, 0.1 V of 3 M sodium acetate (pH 5.2), and 20 μg of glycogen were added to the aqueous solution and incubated at −80°C overnight before centrifuging for 30 min at 12,000 *g* at 4°C. RNA pellets were washed twice with 75% ethanol and dried at room temperature before resuspending in 30 μl of RNase-free water by heating at 55°C for 10 min. Reverse transcription quantitative PCR (RT-qPCR) primers and related probes were designed by Roche Universal ProbeLibrary System Assay Design. The primer sequences and related probes were as follows, unless otherwise specified in other Materials and Methods sections: NUDCD3 (forward: 5′-ACCTTTGACTACCACCAGAAGCTCAGCATCTCATGGACTTTCA-3′) and UPL probe #21, 18*S* ribosomal RNA (forward: 5′-CCGATTGGATGGTTTAGTGAG-3′; reverse: 5′-AGTTCGACCGTCTTCTCAGC-3′) and UPL probe #81, glyceraldehyde-3-phosphate dehydrogenase (GAPDH) (forward: 5′-TGGTATCGTGGAAGGACTCA-3′; reverse: 5′-GCCATCACGCCACAGTTT-3′) and UPL probe #87, and HPRT1 (forward: 5′-TGACCTTGATTTATTTTGCATACC-3′; reverse: 5′-CGAGCAAGACGTTCAGTCCT-3′) and UPL probe #73. Equal amounts of RNA were subjected to qPCR with a Verso one-step RT-qPCR Mix (Thermo Fisher Scientific) and AriaMx Real-time PCR System (Agilent Technologies) according to the manufacturer's instructions.

Radiosensitivity assays

A549 cells were transfected with 200 nM nontargeting siRNA (Thermo Fisher Scientific, 4390843) or siRNA-targeting *NUDCD3* (Thermo Fisher Scientific, Silencer Select s23709, s23710, S2371) using a Neon electroporator (Thermo Fisher Scientific) according to the

Downloaded from https://www.science.org at Leiden University on November 20, 2025

manufacturer's protocol for 48 hours. Transfected A549 cells were then trypsinized and γ-irradiated by using a ^{137}Cs source at a dose rate of 0.04 gray (Gy)/s. Irradiated cells and untreated control cells were split in six-well plates and cultured for 21 days. Wells were exposed to 100 μl of 3-(4,5-dimethylthiazol-2-yl)-2,5-diphenyltetrazolium bromide (MTT) (5 mg/ml) in PBS for 2 hours after 21-day culture. Media then were removed, and 200 μl of isopropanol:HCl (100:1) was added to dissolve MTT. A total of 100 μl of supernatant (containing MTT in isopropanol:HCl) was transferred to a 96-well plate and analyzed at 570 nm to determine cell viability.

Primary dermal fibroblasts (passage 5–9) were trypsinized and irradiated at a dose rate of 0.09 Gy/s before plating onto feeder cells prepared 24 hours earlier. Colony survival was analyzed at 3 weeks.

RAG recombination assay

Recombination assays were performed as described previously (*50*). Briefly, patient fibroblasts (5×10^5) were transfected with 2 μg of pEBB-RAG1, 2 μg of pEBB-RAG2, and 1 μg of pDVG93 substrate plasmids using the Amaxa nucleofection system (Lonza) following the manufacturer's instructions. Cells were transferred to a prewarmed six-well plate containing 2 ml of complete DMEM and incubated for 48 hours. Extrachromosomal DNA was isolated using a modified Hirt prep and eluted in 20 μl of H_2O. After overnight DpnI digestion at 37°C, a qRT-PCR assay was used to detect the amount of substrate plasmid recombination using the primers DG89 (5′-CACAGCAGCGGCCATATCGAAGGTCG-3′) and DG147 (5′-TACATTGAGCAACTGACTGAAATGCC-3′), as well as the probe FM23 (5′-[FAM]CTCCATTTTAGCTTCCTTAGCTCCTG[TAMRA]-3′). This signal was normalized to total levels of transfected pDVG93 that were detected using the primers DpnI-U (5′-GAGCGTCAGACCCCGTAGAA-3′) and DpnI-L (5′-TAGCTCTTGATCCGGCAAACA-3′), as well as the probe T-DpnI (5′-[FAM]TTTCTGCGCGTAATCTGCTGCTTGCA[TAMRA]-3′). Assays were performed in a reaction volume of 25 μl using 2X TaqMan MasterMix (Thermo Fisher Scientific), 300 nM each primer, 100 nM probe, and BSA (0.1 mg/ml) using the following program: 2 min at 50°C, 10 min at 95°C, 50 cycles of 15 s at 95°C, and 1 min at 60°C.

scRNA-seq sample processing and analysis

Cryopreserved peripheral blood mononuclear cells in cryovials were thawed at 37°C and transferred into a 15-ml tube with 10 ml of prewarmed RPMI-1640 medium (Sigma-Aldrich, R0883) supplemented with 10% (v/v) fetal calf serum (FCS) (Gibco, 10270-106), followed by centrifugation at 500*g* for 5 min. The cell pellet was resuspended in 100 μl of cold fluorescence-activated cell sorting (FACS) buffer [PBS + 2% (v/v) FCS + 2 mM EDTA] with a mixture of flow cytometry antibodies. Cells were incubated on ice for 30 min in the dark, washed, and resuspended in FACS buffer. Viability dye 7-amino-actinomycin D (7AAD) was added into cell suspension before cell sorting and analysis on BD FACSAria Fusion (Becton Dickinson). Sorted cell buckets (i) $CD3^+/CD19^+$ and (ii) $CD3^-CD19^-$ were washed. After cell counts were determined, cells were loaded onto each channel of a Chromium chip before encapsulation on the Chromium Controller (10x Genomics). Three sample pools (CTRL_1, RAG2_1, NUDCD3_1) contained 12,000 cells within each cell bucket. One sample pool (RAG1_1 and RAG2_2) was loaded twice for each cell bucket, with 12,000 cells in each load.

For one sample pool (RAG2_1 and NUDCD3_1), 24,000 cells were loaded for each cell bucket. Two sample pools (RAG1_2 and RAG1_6 and CTRL_3 and NUDCD3_2) were loaded twice for each cell bucket, with 16,000 cells in each load. Other sample pools (RAG1_3, RAG1_4, RAG1_5, and NUDCD3_3) had 16,000 cells in each load for each cell bucket.

The single-cell sequencing libraries were generated using the Single Cell 5′ V1 Kit as per the manufacturer's protocol. The 5′ gene expression libraries (for CTRL_1, RAG2_1, NUDCD3_1, and RAG2_1 and NUDCD3_1 for each bucket separately) were sequenced using the Illumina HiSeq 4000 platform, with 10x read parameters: 26–base pair (bp) read 1, 98-bp read 2, 8-bp index 1, and 0-bp index 2. The 5′ gene expression libraries for the rest of samples (RAG1_1 and RAG2_2, RAG1_2 and RAG1_6, CTRL_3 and NUDCD3_2, RAG1_3, RAG1_4, RAG1_5, and NUDCD3_3) were sequenced using the Illumina HiSeq 4000 platform with read parameters 28-bp read 1, 91-bp read 2, 8-bp index 1, and 0-bp index 2. The TCR repertoire was profiled for sorted $CD3^+/CD19^+$ cells along with 5′ gene expression, and these libraries were sequenced using the Illumina HiSeq 4000 platform with read parameters: 150-bp read 1, 150-bp read 2, 8-bp index 1, and 0-bp index 2.

The antibodies used for cell sorting and immunophenotyping are listed in data S2. Flow cytometry data were analyzed by FlowJo V10 (BD Biosciences).

scRNA-seq data analysis

Raw scRNA-seq data coupled with TCR data of two healthy controls from publicly available datasets were used in the analysis of human TCR sequences (*51*, *52*). Raw scRNA-seq data from all 15 samples—including healthy controls and patients with RAG1, RAG2, and NUDCD3—were processed using the Cell Ranger Single-Cell Software Suite (10x Genomics, v3.0.2). Reads were first assigned to cells and then aligned to the human genome using STAR (*53*), with the hg38 build of the human genome (GRCh38_15_plus_hs38d1 + ensembl_90_transcriptome) as a reference for alignment. Results from RNA quantification in Cell Ranger were imported into R (v3.8.1) and analyzed using Seurat (v3) (*54*).

For doublet detection, DoubletFinder (*55*), DoubletDetection (*56*), and Solo (*57*) were applied. Cells were marked as doublets and removed from further analysis if any two algorithms predicted a cell to be a doublet. For eight samples that were pooled together for sequencing in pairs (RAG2_1 and NUDCD3_1, RAG1_1 and RAG2_2, RAG1_2 and RAG1_6, and CTRL_3 and NUDCD3_2), cellSNP v0.1.6 and vireoSNP v0.1.3 were used to additionally deconvolute doublets on the basis of genotypes and WES data (*58*, *59*).

For quality control, normalization, and data scaling, cells that expressed fewer than 300 genes or in which we detected more than 10% unique molecular identifiers (UMIs) from mitochondrial transcripts or fewer than 200 UMIs were first excluded. Data were normalized for library size and log-transformed using default Seurat parameters with NormalizeData function. A publicly available list of cell-cycle genes (*60*) was used to perform cell-cycle scoring and to assign cells to their respective stage of the cell cycle using Seurat CellCycleScoring function. The data were then normalized with Seurat's SCTransform with default parameters, regressing out the following covariates: number of expressed genes per cell, number of UMIs per cell, proportion of transcripts mapping to mitochondrial genes, and cell cycle score.

For the eight samples (RAG2_1, NUDCD3_1, RAG1_1, RAG1_2, RAG1_6, RAG2_2, CTRL_3, and NUDCD3_2) that were sequenced in two batches, sequencing runs were integrated with Seurat::IntegrateData using all genes as integration anchors.

Downloaded from https://www.science.org at Leiden University on November 20, 2025

Batch-corrected counts provided in the integrated slot of the Seurat data object were used for further analysis.

Next, for each cell bucket ($CD3^+$/$CD19^+$ and $CD3^-CD19^-$) separately, we integrated all cells from all 15 samples together with Seurat::IntegrateData. The integration was performed on 5000 highly variable anchor genes (excluding mitochondrial transcripts, genes coding TRA and TRB, ribosomal proteins, *AL138963*, *AL133415*, and *MALAT1* because they correlate with cell viability and TCR specificity rather than with cell type). Principal components analysis (PCA) with Seurat::RunPCA and uniform manifold approximation and projection (UMAP) with Seurat::RunUMAP using the first 25 principal components (PCs) were computed. Then, cells were clustered using the first 25 PCs with shared nearest neighbor (SNN) modularity optimization-based clustering algorithm implemented Seurat::FindNeighbors and Seurat::FindClusters, testing for optimal resolution parameter (0.1 to 1.5, step = 0.1).

After the first round of cell clustering, each cell from the lymphoid bucket was annotated as either T cell or B cell, whereas each cell from the myeloid bucket was annotated as monocyte, NK cell, dendritic cell, or other (Fig. 2 and figs. S5 and S6). T and B cells were identified on the basis of expression of T cell markers (*CD3D*, *CD3E*, and *CD3G*) and B cell markers (*CD19*, *CD74A*, and *MS4A1*). T cell clusters were further annotated into CD4 T cell subsets ($CD4^+$), CD8 T cells ($CD8A^+$ and $CD8B^+$), γδ T cells ($TRDV^+$ and $TRGV^+$), and mucosal-associated invariant T (MAIT) cells ($TRAV1–2^+$ and $TRAJ12/20/33^+$). Monocytes were differentiated from NK and dendritic cells on the basis of CD14 and CD16 marker expression, whereas NK cells were characterized by high expression of *NCAM1*, *NKG7*, and *GNLY* coupled with expression of chemokines (*CCL4* and *CCL5*) and granzymes (*GZMK* and *GZMB*). Dendritic cells were annotated on the basis of *FCER1A*, *CD74*, and *CD1C* expression.

To increase the accuracy of cell-type annotation, a second round of dimensionality reduction and clustering was performed in which each of the six cell populations (all lymphoid cells, CD4 T cells, CD8 T cells, γδ T cells, all myeloid cells, and monocytes) were analyzed separately. Resulting clusters were annotated using known cell type–specific gene markers and cluster-specific genes that were identified using the Wilcoxon rank-sum test (figs. S5 and S6). The Mann-Whitney *U* test was used to compare frequencies of the annotated cell subtypes between patients on the basis of the mutation gene group: (i) *NUDCD3* and (ii) *RAG1*- and *RAG2*-deficient and healthy individuals. Owing to the small sample sizes and broad similarity between (i) and (ii), we grouped all patients with OS together to perform pairwise comparisons with healthy controls to assess for statistical differences in cell subtype proportions. A nonparametric test was used for pairwise comparisons between patient groups and controls because normality of distribution cannot be established given the extremely small sample size. To account for multiple testing, FDR correction was applied to all *P* values obtained in pairwise comparisons between patients with OS and healthy controls.

For single-cell TCR analysis, raw TCR FASTQ reads were processed with a patched version of Cell Ranger v3.0.2 provided by 10x Genomics. We used GRCh38-alts-ensembl-3.1.0 V(D)J reference to obtain TRA, TRB, and clonotype assignment. Shannon entropy (H) was estimated for TRA and TRB chains separately, for productive sequences only, as

$$H = -\sum_{i=1}^{S} p_i \log p_i$$

where p_i was a proportion of clonotype i and S was a number of clonotypes in repertoire.

In the tree plots, each sample is represented as a set of rectangles corresponding to unique clonotypes. Rectangle size is proportional to the number of cells with this clonotype. Colors are applied to help distinguish different clonotypes within a sample, and rectangles of the same color do not represent the same clonotype.

KREC assay

103/BCL-2 pre-B cells were transfected with *Nudcd3*-targeting or nontargeting siRNA (Thermo Fisher Scientific, Silencer Select s102125, s102126, s102127) using the mouse B cell nucleofector kit in conjunction with the Amaxa nucleofection system (Lonza) according to the manufacturer's instructions. Transfected cells were cultured in antibiotic free media in the wells of 12-well plates at 33°C for 48 hours to allow sufficient knockdown. Plates were then transferred to 39°C or retained at 33°C for a further 48 hours. After this incubation period, cells were harvested and total DNA and total RNA were extracted using the QIAamp DNA Mini Kit (QIAGEN) and ReliaPrep RNA miniprep system (Promega), respectively, according to the manufacturer's instructions. KRECs were detected using a qPCR assay with a 900 nM final primer concentration and a 100 nM final probe concentration. The KREC assay signal (forward: 5′-CTCCAATAAGTCACCCTTTCCTTGT-3′; reverse, 5′-GGAGTGGATTCAGGACACTGCT-3′ and probe 5′-[FAM]CCAGTTTCTGCACGGGCAGTCAGTTAG[TAMRA]-3′) was normalized to the signal from a genomic albumin assay (forward: 5′-TCACCTTTCCTATCAACCCCA-3′; reverse: 5′-CGAAACACACCCCTGGAAAA-3′ and probe 5′-[FAM]TCTCCTCCTCCTCTTCGTCT[TAMRA]-3′). RNA from the same cells was used to synthesize cDNA using the M-MLV reverse transcriptase according to the manufacturer's instructions (Promega). Template cDNA (5 μl) was used in a final volume of 20 μl using 2X SYBR Green Master Mix (no ROX) (Bioline) and 400 nM of each primer. Assays for murine *Nudcd3* (forward: 5′-TTCGGCTTTCTCTACCGCAA-3′; reverse: 5′-CCTTGGCCTCTTCCTCCTTT-3′) and the housekeeping gene *Hprt1* (forward: 5′-CAAACTTTGCTTTCCCTGGT-3′; reverse: 5′-TCTGGCCTGTATCCAACACTTC-3′) were performed using the following program: 2 min at 95°C, 40 cycles of 5 s at 95°C, 10 s at 60°C, 20 s at 72°C, and a melt-curve step to check for multiple PCR products.

Mouse strains

The $Nudcd3^{em1(IMPC)Wtsi}$ mice on a C57BL/6N6NTac/USA background (referred to as $Nudcd3^{Hom}$ in the homozygous state) were generated by the Wellcome Trust Genome Campus (Hinxton, UK) by CRISPR-Cas9 editing using the guide RNA sequence 5′-CGCCACCCTTCGGACCGCAT-3′ and template DNA sequence 5′-GCCCGCCGCCTCTCTCCACCTCACCTGCAGCACCAGGGCCTGTGCGGCCCCGGGCGGGAAGTCCATGCGGTCCGAAGGGTGGCGCAGCAGGCGGTAGAAGTCGGTCTTGCGGT-3′ (Fig. 3A). Heterozygous $Nudcd3^{Hom}$ (referred to hereafter as $Nudcd3^{Het}$) mice were subjected to the International Mouse Phenotyping Consortium (IMPC) phenotyping process (*61*). All mice were housed in barrier facilities at Comparative Biology Centre (CBC), Newcastle University, UK. All experimental procedures were approved by CBC Newcastle University local authorities and were performed in accordance with UK Home Office regulations. All mice were housed in groups of seven maximum with a 12-hour

Downloaded from https://www.science.org at Leiden University on November 20, 2025

light/12-hour dark cycle and provided food and water ad libitum. *Nudcd3*^{Het} mice were bred to generate homozygous *Nudcd3*^{Hom} mice. Progeny mice were genotyped from ear notches taken at postnatal day 14 (P14). DNA was isolated using a DNeasy Blood & Tissue Kit (QIAGEN) and the "Purification of Total DNA from Animal Tissues (Spin-Column Protocol)." DNA was amplified by PCR using the following primers: forward: 5′-CAATCAGCCGGTGTGAGGCG-3′ and reverse: 5′-GGGTTTGTGATTCTCTCTGG-3′ in the following reaction volumes: 10 μl of 5X MyTaq reaction buffer, 2 μl of each primer, 2 μl of template, 0.5 μl of MyTaq HS DNA Polymerase (5000 U/ml) (Meridian, BIO-21112), and 33.5 μl of water for a total volume of 60 μl. The following PCR program was used: 1 min at 95°C, 37 cycles of 15 s at 95°C, 15 s at 57°C, 30 s at 72°C, 5 min at 72°C, and 10 min at 10°C on an Alpha Cycler 1 PCRmax machine. Sanger sequencing was performed by Eurofins Genomics using the following primer: 5′-CCAGAGAGAATCACAAACCC-3′.

The congenic strain of BoyJ mice used in mixed BM chimera experiments (see below) was Ly5.1 Mouse (B6.SJL-PtprcaPepcb/BoyCrl) purchased from Charles River Laboratories. Host recipients used in mixed chimeras were a double-fluorescent Cre-reporter mouse with universal expression of membrane-targeted tdTomato (mT) before Cre excision and membrane-targeted EGFP (mG) after Cre excision (sourced from the Jackson Laboratory) (*62*). These mice were housed at the University of Birmingham Biomedical Services Unit. All experimental procedures were approved by the Birmingham Animal Welfare and Ethical Review Body and were performed in accordance with UK Home Office regulations.

Flow cytometry (mouse)

Mice were weighed before being euthanized at 5 to 8 weeks of age by injecting 100 μl of Euthatal (200 mg/ml) (pentobarbitone injectable, Dipharma) intraperitoneally. Blood was then collected using cardiac puncture and diluted with 100 μl of heparin (5000 IU/ml). Death was confirmed by cervical dislocation. Female and male animals were pooled in the analysis except when comparing weight and thymic cellularity. For these readouts, only 5- to 12-week-old males were analyzed. Some younger (3 weeks) and older animals (40 weeks) from pilot studies were also included. The reduced Mendelian ratios of homozygous animals born to heterozygous breeding pairs meant that one litter of six to eight mice often only included one homozygous pup. Animals were analyzed in triplicate alongside littermate controls (*Nudcd3*^{WT}, *Nudcd3*^{Het}, or *Nudcd3*^{Hom}) where possible. If two litter triplicates were 5 to 8 weeks old simultaneously, they were phenotyped on the same day. Details of independent replicates of each experiment can be found in data S3. Thymi, spleens, and clavicular, axillary, and mesenteric lymph nodes were isolated by blunt dissection and transferred to cold Iscove's modified Dulbecco's medium (IMDM) with 0.1% BSA (v/v). Femurs were isolated by cutting just above the hip and below the knee joint. Thymocytes and lymphocytes were isolated by mechanically dissociating the thymi, spleens, and lymph nodes either between two sections of nylon mesh (70 μm in diameter) or between two glass slides. Single-cell suspensions were counted on a Tali Image Cytometer (Thermo Fisher Scientific, USA) or using counting beads (Spherotech AccuCount beads ACBP-100-10). Blood was lysed in ammonium-chloride-potassium (ACK) lysis buffer (dH_2O with 150 mM NH_4Cl, 10 mM $KHCO_3$, and 0.1 mM EDTA) for 3 min at room temperature. Single cells were washed and resuspended in cold FACS buffer (PBS (Gibco) with 5 to 10% FCS and 0.5% sodium azide or PBS (Gibco) with or without $CaCl_2$ and $MgCl_2$) at a concentration of 0.5×10^6 to 5×10^6 cells per 100 μl with specific surface antibodies on a rocker in a dark cold room (4°C) for at least 30 min. For analysis of DN and early T cell progenitor populations, 10^7 cells were stained with 100 μl of antibody mix. Cells were either stained with a viability dye before surface staining (Fixable Dead Cell Stain Kit Zombie Aqua from Invitrogen) or just before acquisition (1:2000; DAPI). The antibodies used are listed in data S2. Foxp3 and Ki67 staining were performed using an intracellular Foxp3 kit purchased from eBioscience (00-5523-00). Streptavidin BV786 (BD Horizon) (1:100) was used to reveal staining with biotinylated antibodies. iNKT cells were identified using unloaded PBS57-loaded CD1d tetramers (obtained from the National Institutes of Health Tetramer Facility). Samples were analyzed using the BD FACSymphony A5 or the BD LSRFortessa X20 running BD FACSDiva software followed by analysis in FlowJo V10 (BD Biosciences) and Graphpad Prism 8 or 9. Comparison of population frequency (frequency of parent) or cell number (frequency of total × organ cellularity counted as above) was performed using analysis of variance (ANOVA) (Bonferroni and alpha threshold set at 0.05) unless otherwise specified. Only statistically significant differences are marked in the figures.

Generation of mixed BM chimeras

Host recipients used in mixed chimeras were a double-fluorescent Cre reporter mouse with universal expression of membrane-targeted tdTomato (mT) before Cre excision and membrane-targeted EGFP (mG) after Cre excision (sourced from the Jackson Laboratory) (*62*) to allow the identification of host cells (mT^+) (fig. S10K). Recipient mice were lethally irradiated (2 × 5 gray) and reconstituted intravenously with 5×10^6 T cell–depleted adult BM preparations made from CD45.2 congenically marked *Nudcd3*^{WT} or *Nudcd3*^{Hom} cells mixed at a 1:1 ratio with CD45.1 congenically marked WT cells isolated from BoyJ mice. Depletion of T cells was performed using anti–CD3–phycoerythrin (PE) and anti-PE microbeads (Miltenyi Biotec) according to the manufacturer's instructions. Mice were euthanized 28 days after reconstitution, and tissues were analyzed by flow cytometry described above. The antibodies used in addition to the panels described above are listed in data S2.

Mouse TCR/BCR repertoire by 5′ RACE and analysis

RNA was extracted from approximately 20 mg of sliced and macerated mouse spleen that was snap-frozen in liquid N_2 upon isolation using the RNeasy Plus Mini Kit (QIAGEN, Germany) following the manufacturer's protocol. RNA concentration and quality (RNA integrity number) were determined by the Agilent RNA 6000 Nano Kit using Agilent 2100 Bioanalyzer. Mouse TCR and BCR libraries were prepared using SMARTer Mouse TCR a/b Profiling Kit and SMARTer Mouse BCR IgG H/K/L Profiling Kit (Takara Bio USA, Inc.) following the manufacturer's protocol. Concentration and quality of DNA libraries were determined by Agilent DNA 1000 Kit using Agilent 2100 Bioanalyzer. TCR and BCR libraries were pooled before being sequenced by Illumina MiSeq Platform using MiSeq Reagent Kit v3 (2 × 300 bp, 600 cycles). Bioinformatic analysis is described as follows.

Receptors were reconstructed and quantified from raw FASTQ reads with MIXCR (v3.0.3, built-in V/D/J/C library: repseqio.v1.5) with default settings. TCRs with CDR3 containing stop codon or frameshift mutation were assigned nonproductive status. Diversity estimates were obtained as for human sequences, with productive sequences only.

Downloaded from https://www.science.org at Leiden University on November 20, 2025

Mouse immunoglobulin ELISA

Mouse whole blood was left undisturbed at room temperature for 30 min to clot and then centrifuged at 1000*g* for 10 min at 4°C. The resulting serum supernatant was collected for enzyme-linked immunosorbent assay (ELISA). The serum was diluted, and ELISAs were performed using the following kits: Abcam Mouse IgA ELISA Kit (ab157717), Abcam Mouse IgG1 ELISA Kit (ab133045), Invitrogen Mouse IgG2a ELISA Kit (88-50420-22), Invitrogen Mouse IgG2b ELISA Kit (88-50430-22), Invitrogen Mouse IgG3 ELISA Kit (88-50440-22), Invitrogen Mouse IgM ELISA Kit (88-50470-22), Invitrogen Mouse IgE ELISA Kit (88-50460-22) and according to the manufacturer's instructions. The results were read using Tecan Sunrise Microplate Reader.

Mouse pre-B cell in vitro recombination assay

Heterogenous mononuclear BM cells were first infected with Bcl2 retrovirus or coinfected by Bcl2 and v-Abl retroviruses as described above. Transduced cells were initially cultured in BM media supplemented with IL-7 (10 ng/ml; BioLegend) for 7 days. v-Abl pre-B cells were then maintained without IL-7 supplement and infected with pMGINV reporter virus for 72 hours and subsequently treated with 5 μM imatinib (Sigma-Aldrich) for 48 hours to trigger recombination. GFP-positive cells were evaluated using flow cytometry.

Statistics

Statistical analysis and verification of normal distribution were conducted using GraphPad Prism software except in the case of single-cell transcriptomic analysis (see below). For comparisons between groups, a one-sample *t* test, an unpaired Student's *t* test, or a one-way or two-way ANOVA with Bonferroni post hoc multiple comparisons test was used as appropriate and as described in the figure legends. Data (biological replicates) are presented as the 25th to 75th percentiles with line at median or means ± SEM as described in the figure legends. $P < 0.05$ is considered as significant. In all figures, $*P < 0.05$, $**P < 0.01$, $***P < 0.001$, and $****$ $P < 0.0001$.

For single-cell transcriptomic analysis, the Mann-Whitney *U* test to compare frequencies of annotated cell subtypes between patients and healthy individuals was conducted in Python (v3.10) using the stats.mannwhitneyu function from the SciPy (v1.8.0) library. The Wilcoxon rank-sum test to identify cluster-specific genes during single-cell data analysis was conducted in R (v3.8.1) with the Seurat (v3) package using FindMarkers or FindConservedMarkers functions applied to Seurat data objects.

Supplementary Materials

This PDF file includes:

Figs. S1 to S15
Tables S1 to S6
References (*64*–*72*)

Other Supplementary Material for this manuscript includes the following:

Data files S1 to S5
MDAR Reproducibility Checklist

REFERENCES AND NOTES

1. A. Fischer, L. D. Notarangelo, B. Neven, M. Cavazzana, J. M. Puck, Severe combined immunodeficiencies and related disorders. *Nat. Rev. Dis. Primers* **1**, 15061 (2015).
2. S. G. Tangye, W. Al-Herz, A. Bousfiha, C. Cunningham-Rundles, J. L. Franco, S. M. Holland, C. Klein, T. Morio, E. Oksenhendler, C. Picard, A. Puel, J. Puck, M. R. J. Seppanen, R. Somech, H. C. Su, K. E. Sullivan, T. R. Torgerson, I. Meyts, Human inborn errors of immunity: 2022 update on the classification from the International Union of Immunological Societies Expert Committee. *J. Clin. Immunol.* **42**, 1473–1507 (2022).
3. A. Villa, L. D. Notarangelo, C. M. Roifman, Omenn syndrome: Inflammation in leaky severe combined immunodeficiency. *J. Allergy Clin. Immunol.* **122**, 1082–1086 (2008).
4. J. M. Puck, Newborn screening for severe combined immunodeficiency and T-cell lymphopenia. *Immunol. Rev.* **287**, 241–252 (2019).
5. J. P. de Villartay, Congenital defects in V(D)J recombination. *Br. Med. Bull.* **114**, 157–167 (2015).
6. C. Liu, Y. Zhang, C. C. Liu, D. G. Schatz, Structural insights into the evolution of the RAG recombinase. *Nat. Rev. Immunol.* **22**, 353–370 (2022).
7. G. Teng, D. G. Schatz, Regulation and evolution of the RAG recombinase. *Adv. Immunol.* **128**, 1–39 (2015).
8. L. Zhang, T. L. Reynolds, X. Shan, S. Desiderio, Coupling of V(D)J recombination to the cell cycle suppresses genomic instability and lymphoid tumorigenesis. *Immunity* **34**, 163–174 (2011).
9. A. R. Gennery, E. Hodges, A. P. Williams, S. Harris, A. Villa, B. Angus, A. J. Cant, J. L. Smith, Omenn's syndrome occurring in patients without mutations in recombination activating genes. *Clin. Immunol.* **116**, 246–256 (2005).
10. A. Stray-Pedersen, H. S. Sorte, P. Samarakoon, T. Gambin, I. K. Chinn, Z. H. C. Akdemir, H. C. Erichsen, L. R. Forbes, S. Gu, B. Yuan, S. N. Jhangiani, D. M. Muzny, O. K. Rodningen, Y. Sheng, S. K. Nicholas, L. M. Noroski, F. O. Seeborg, C. M. Davis, D. L. Canter, E. M. Mace, T. J. Vece, C. E. Allen, H. A. Abhyankar, P. M. Boone, C. R. Beck, W. Wiszniewski, B. Fevang, P. Aukrust, G. E. Tjonnfjord, T. Gedde-Dahl, H. Hjorth-Hansen, I. Dybedal, I. Nordoy, S. F. Jorgensen, T. G. Abrahamsen, T. Overland, A. G. Bechensteen, V. Skogen, L. T. N. Osnes, M. A. Kulseth, T. E. Prescott, C. F. Rustad, K. R. Heimdal, J. W. Belmont, N. L. Rider, J. Chinen, T. N. Cao, E. A. Smith, M. S. Caldirola, L. Bezrodnik, S. O. L. Reyes, F. J. E. Rosales, N. D. Guerrero-Cursaru, L. A. Pedroza, C. M. Poli, J. L. Franco, C. M. T. Vargas, J. C. A. Becerra, N. Wright, T. B. Issekutz, A. C. Issekutz, J. Abbott, J. W. Caldwell, D. K. Bayer, A. Y. Chan, A. Aiuti, C. Cancrini, E. Holmberg, C. West, M. Burstedt, E. Karaca, G. Yesil, H. Artac, Y. Bayram, M. M. Atik, M. K. Eldomery, M. S. Ehlayel, S. Jolles, B. Flato, A. A. Bertuch, I. C. Hanson, V. W. Zhang, L. J. Wong, J. Hu, M. Walkiewicz, Y. Yang, C. M. Eng, E. Boerwinkle, R. A. Gibbs, W. T. Shearer, R. Lyle, J. S. Orange, J. R. Lupski, Primary immunodeficiency diseases: Genomic approaches delineate heterogeneous Mendelian disorders. *J. Allergy Clin. Immunol.* **139**, 232–245 (2017).
11. GenomeAsia100k Consortium, The GenomeAsia 100K Project enables genetic discoveries across Asia. *Nature* **576**, 106–111 (2019).
12. K. J. Karczewski, L. C. Francioli, G. Tiao, B. B. Cummings, J. Alfoldi, Q. Wang, R. L. Collins, K. M. Laricchia, A. Ganna, D. P. Birnbaum, L. D. Gauthier, H. Brand, M. Solomonson, N. A. Watts, D. Rhodes, M. Singer-Berk, E. M. England, E. G. Seaby, J. A. Kosmicki, R. K. Walters, K. Tashman, Y. Farjoun, E. Banks, T. Poterba, A. Wang, C. Seed, N. Whiffin, J. X. Chong, K. E. Samocha, E. Pierce-Hoffman, Z. Zappala, A. H. O'Donnell-Luria, E. V. Minikel, B. Weisburd, M. Lek, J. S. Ware, C. Vittal, I. M. Armean, L. Bergelson, K. Cibulskis, K. M. Connolly, M. Covarrubias, S. Donnelly, S. Ferriera, S. Gabriel, J. Gentry, N. Gupta, T. Jeandet, D. Kaplan, C. Llanwarne, R. Munshi, S. Novod, N. Petrillo, D. Roazen, V. Ruano-Rubio, A. Saltzman, M. Schleicher, J. Soto, K. Tibbetts, C. Tolonen, G. Wade, M. E. Talkowski, Genome Aggregation Database Consortium, B. M. Neale, M. J. Daly, D. G. MacArthur, The mutational constraint spectrum quantified from variation in 141,456 humans. *Nature* **581**, 434–443 (2020).
13. I. A. Adzhubei, S. Schmidt, L. Peshkin, V. E. Ramensky, A. Gerasimova, P. Bork, A. S. Kondrashov, S. R. Sunyaev, A method and server for predicting damaging missense mutations. *Nat. Methods* **7**, 248–249 (2010).
14. M. Kircher, D. M. Witten, P. Jain, B. J. O'Roak, G. M. Cooper, J. Shendure, A general framework for estimating the relative pathogenicity of human genetic variants. *Nat. Genet.* **46**, 310–315 (2014).
15. Y. Wu, R. Li, S. Sun, J. Weile, F. P. Roth, Improved pathogenicity prediction for rare human missense variants. *Am. J. Hum. Genet.* **108**, 1891–1906 (2021).
16. Q. Fu, W. Wang, T. Zhou, Y. Yang, Emerging roles of NudC family: From molecular regulation to clinical implications. *Sci. China Life Sci.* **59**, 455–462 (2016).
17. M. E. Rebeaud, S. Mallik, P. Goloubinoff, D. S. Tawfik, On the evolution of chaperones and cochaperones and the expansion of proteomes across the Tree of Life. *Proc. Natl. Acad. Sci. U.S.A.* **118**, e2020885118 (2021).
18. M. Taipale, G. Tucker, J. Peng, I. Krykbaeva, Z. Y. Lin, B. Larsen, H. Choi, B. Berger, A. C. Gingras, S. Lindquist, A quantitative chaperone interaction network reveals the architecture of cellular protein homeostasis pathways. *Cell* **158**, 434–448 (2014).
19. M. M. Biebl, F. Delhommel, O. Faust, K. M. Zak, G. Agam, X. Guo, M. Muhlhofer, V. Dahiya, D. Hillebrand, G. M. Popowicz, M. Kampmann, D. C. Lamb, R. Rosenzweig, M. Sattler, J. Buchner, NudC guides client transfer between the Hsp40/70 and Hsp90 chaperone systems. *Mol. Cell* **82**, 555–569.e7 (2022).
20. Y. Yang, W. Wang, M. Li, Y. Gao, W. Zhang, Y. Huang, W. Zhuo, X. Yan, W. Liu, F. Wang, D. Chen, T. Zhou, NudCL2 is an Hsp90 cochaperone to regulate sister chromatid cohesion by stabilizing cohesin subunits. *Cell. Mol. Life Sci.* **76**, 381–395 (2019).

Downloaded from https://www.science.org at Leiden University on November 20, 2025

21. T. Zhou, W. Zimmerman, X. Liu, R. L. Erikson, A mammalian NudC-like protein essential for dynein stability and cell viability. *Proc. Natl. Acad. Sci. U.S.A.* **103**, 9039–9044 (2006).
22. Y. Cai, Y. Yang, M. Shen, T. Zhou, Inhibition of cytokinesis by overexpression of NudCL that is localized to the centrosome and midbody. *Cell Res.* **19**, 1305–1308 (2009).
23. C. Suo, E. Dann, I. Goh, L. Jardine, V. Kleshchevnikov, J. E. Park, R. A. Botting, E. Stephenson, J. Engelbert, Z. K. Tuong, K. Polanski, N. Yayon, C. Xu, O. Suchanek, R. Elmentaite, C. Dominguez Conde, P. He, S. Pritchard, M. Miah, C. Moldovan, A. S. Steemers, P. Mazin, M. Prete, D. Horsfall, J. C. Marioni, M. R. Clatworthy, M. Haniffa, S. A. Teichmann, Mapping the developing human immune system across organs. *Science* **376**, eabo0510 (2022).
24. J. E. Park, R. A. Botting, C. Dominguez Conde, D. M. Popescu, M. Lavaert, D. J. Kunz, I. Goh, E. Stephenson, R. Ragazzini, E. Tuck, A. Wilbrey-Clark, K. Roberts, V. R. Kedlian, J. R. Ferdinand, X. He, S. Webb, D. Maunder, N. Vandamme, K. T. Mahbubani, K. Polanski, L. Mamanova, L. Bolt, D. Crossland, F. de Rita, A. Fuller, A. Filby, G. Reynolds, D. Dixon, K. Saeb-Parsy, S. Lisgo, D. Henderson, R. Vento-Tormo, O. A. Bayraktar, R. A. Barker, K. B. Meyer, Y. Saeys, P. Bonfanti, S. Behjati, M. R. Clatworthy, T. Taghon, M. Haniffa, S. A. Teichmann, A cell atlas of human thymic development defines T cell repertoire formation. *Science* **367**, eaay3224 (2020).
25. A. Tsherniak, F. Vazquez, P. G. Montgomery, B. A. Weir, G. Kryukov, G. S. Cowley, S. Gill, W. F. Harrington, S. Pantel, J. M. Krill-Burger, R. M. Meyers, L. Ali, A. Goodale, Y. Lee, G. Jiang, J. Hsiao, W. F. J. Gerath, S. Howell, E. Merkel, M. Ghandi, L. A. Garraway, D. E. Root, T. R. Golub, J. S. Boehm, W. C. Hahn, Defining a cancer dependency map. *Cell* **170,** 564–576 (2017).
26. A. Berland, J. Rosain, S. Kaltenbach, V. Allain, N. Mahlaoui, I. Melki, A. Fievet, C. Dubois d'Enghien, M. Ouachee-Chardin, L. Perrin, N. Auger, F. E. Cipe, A. Finocchi, F. Dogu, F. Suarez, D. Moshous, T. Leblanc, A. Belot, C. Fieschi, D. Boutboul, M. Malphettes, L. Galicier, E. Oksenhendler, S. Blanche, A. Fischer, P. Revy, D. Stoppa-Lyonnet, C. Picard, J. P. de Villartay, PROMIDISα: A T-cell receptor α signature associated with immunodeficiencies caused by V(D)J recombination defects. *J. Allergy Clin. Immunol.* **143**, 325–334.e2 (2019).
27. D. Brandle, C. Muller, T. Rulicke, H. Hengartner, H. Pircher, Engagement of the T-cell receptor during positive selection in the thymus down-regulates RAG-1 expression. *Proc. Natl. Acad. Sci. U.S.A.* **89**, 9529–9533 (1992).
28. Y. N. Lee, F. Frugoni, K. Dobbs, I. Tirosh, L. Du, F. A. Ververs, H. Ru, L. Ott de Bruin, M. Adeli, J. H. Bleesing, D. Buchbinder, M. J. Butte, C. Cancrini, K. Chen, S. Choo, R. A. Elfeky, A. Finocchi, R. L. Fuleihan, A. R. Gennery, D. H. El-Ghoneimy, L. A. Henderson, W. Al-Herz, E. Hossny, R. P. Nelson, S. Y. Pai, N. C. Patel, S. M. Reda, P. Soler-Palacin, R. Somech, P. Palma, H. Wu, S. Giliani, J. E. Walter, L. D. Notarangelo, Characterization of T and B cell repertoire diversity in patients with RAG deficiency. *Sci. Immunol.* **1**, eaah6109 (2016).
29. X. Yu, J. R. Almeida, S. Darko, M. van der Burg, S. S. DeRavin, H. Malech, A. Gennery, I. Chinn, M. L. Markert, D. C. Douek, J. D. Milner, Human syndromes of immunodeficiency and dysregulation are characterized by distinct defects in T-cell receptor repertoire development. *J. Allergy Clin. Immunol.* **133**, 1109–1115.e14 (2014).
30. Y. Y. Chen, L. C. Wang, M. S. Huang, N. Rosenberg, An active v-abl protein tyrosine kinase blocks immunoglobulin light-chain gene rearrangement. *Genes Dev.* **8**, 688–697 (1994).
31. S. Takeda, Y. R. Zou, H. Bluethmann, D. Kitamura, U. Muller, K. Rajewsky, Deletion of the immunoglobulin kappa chain intron enhancer abolishes kappa chain gene rearrangement in cis but not lambda chain gene rearrangement in trans. *EMBO J.* **12**, 2329–2336 (1993).
32. M. van der Burg, T. Tumkaya, M. Boerma, S. de Bruin-Versteeg, A. W. Langerak, J. J. van Dongen, Ordered recombination of immunoglobulin light chain genes occurs at the IGK locus but seems less strict at the IGL locus. *Blood* **97**, 1001–1008 (2001).
33. K. Khiong, M. Murakami, C. Kitabayashi, N. Ueda, S. Sawa, A. Sakamoto, B. L. Kotzin, S. J. Rozzo, K. Ishihara, M. Verella-Garcia, J. Kappler, P. Marrack, T. Hirano, Homeostatically proliferating CD4 T cells are involved in the pathogenesis of an Omenn syndrome murine model. *J. Clin. Invest.* **117**, 1270–1281 (2007).
34. V. Marrella, P. L. Poliani, A. Casati, F. Rucci, L. Frascoli, M. L. Gougeon, B. Lemercier, M. Bosticardo, M. Ravanini, M. Battaglia, M. G. Roncarolo, M. Cavazzana-Calvo, F. Facchetti, L. D. Notarangelo, P. Vezzoni, F. Grassi, A. Villa, A hypomorphic R229Q Rag2 mouse mutant recapitulates human Omenn syndrome. *J. Clin. Invest.* **117**, 1260–1269 (2007).
35. L. M. Ott de Bruin, M. Bosticardo, A. Barbieri, S. G. Lin, J. H. Rowe, P. L. Poliani, K. Ching, D. Eriksson, N. Landegren, O. Kampe, J. P. Manis, L. D. Notarangelo, Hypomorphic Rag1 mutations alter the preimmune repertoire at early stages of lymphoid development. *Blood* **132**, 281–292 (2018).
36. U. Koch, F. Radtke, Mechanisms of T cell development and transformation. *Annu. Rev. Cell Dev. Biol.* **27**, 539–562 (2011).
37. T. Taghon, M. A. Yui, R. Pant, R. A. Diamond, E. V. Rothenberg, Developmental and molecular characterization of emerging β- and γδ-selected pre-T cells in the adult mouse thymus. *Immunity* **24**, 53–64 (2006).
38. P. Matangkasombut, M. Pichavant, D. E. Saez, S. Giliani, E. Mazzolari, A. Finocchi, A. Villa, C. Sobacchi, P. Cortes, D. T. Umetsu, L. D. Notarangelo, Lack of iNKT cells in patients with combined immune deficiency due to hypomorphic RAG mutations. *Blood* **111**, 271–274 (2008).
39. A. Bendelac, P. B. Savage, L. Teyton, The biology of NKT cells. *Annu. Rev. Immunol.* **25**, 297–336 (2007).
40. R. M. Brecht, C. C. Liu, H. A. Beilinson, A. Khitun, S. A. Slavoff, D. G. Schatz, Nucleolar localization of RAG1 modulates V(D)J recombination activity. *Proc. Natl. Acad. Sci. U.S.A.* **117**, 4300–4309 (2020).
41. E. Spanopoulou, P. Cortes, C. Shih, C. M. Huang, D. P. Silver, P. Svec, D. Baltimore, Localization, interaction, and RNA binding properties of the V(D)J recombination-activating proteins RAG1 and RAG2. *Immunity* **3**, 715–726 (1995).
42. T. Gan, Y. Wang, Y. Liu, D. G. Schatz, J. Hu, RAG2 abolishes RAG1 aggregation to facilitate V(D)J recombination. *Cell Rep.* **37**, 109824 (2021).
43. P. Banski, M. Kodiha, U. Stochaj, Chaperones and multitasking proteins in the nucleolus: Networking together for survival? *Trends Biochem. Sci.* **35**, 361–367 (2010).
44. F. Frottin, F. Schueder, S. Tiwary, R. Gupta, R. Korner, T. Schlichthaerle, J. Cox, R. Jungmann, F. U. Hartl, M. S. Hipp, The nucleolus functions as a phase-separated protein quality control compartment. *Science* **365**, 342–347 (2019).
45. J. L. Marin-Rubio, R. E. Peltier-Heap, M. E. Duenas, T. Heunis, A. Dannoura, J. Inns, J. Scott, A. J. Simpson, H. J. Blair, O. Heidenreich, J. M. Allan, J. E. Watt, M. P. Martin, B. Saxty, M. Trost, A matrix-assisted laser desorption/ionization time-of-flight assay identifies nilotinib as an inhibitor of inflammation in acute myeloid leukemia. *J. Med. Chem.* **65**, 12014–12030 (2022).
46. J. Cox, M. Mann, MaxQuant enables high peptide identification rates, individualized p.p.b.-range mass accuracies and proteome-wide protein quantification. *Nat. Biotechnol.* **26**, 1367–1372 (2008).
47. UniProt Consortium, UniProt: The Universal Protein Knowledgebase in 2023. *Nucleic Acids Res.* **51**, D523–D531 (2023).
48. UniProt search results; www.uniprot.org/uniprotkb?query=Human&facets=reviewed%3Atrue%2C model_organism%3A9606.
49. M. E. Ritchie, B. Phipson, D. Wu, Y. Hu, C. W. Law, W. Shi, G. K. Smyth, limma powers differential expression analyses for RNA-sequencing and microarray studies. *Nucleic Acids Res.* **43**, e47 (2015).
50. M. van der Burg, N. S. Verkaik, A. T. den Dekker, B. H. Barendregt, I. Pico-Knijnenburg, I. Tezcan, J. J. M. vanDongen, D. C. van Gent, Defective Artemis nuclease is characterized by coding joints with microhomology in long palindromic-nucleotide stretches. *Eur. J. Immunol.* **37**, 3522–3528 (2007).
51. D. Dixon, "Effects of STAT3 gain of function on myeloid cells in human peripheral blood mononuclear cells," thesis, Newcastle University, Newcastle upon Tyne (2020).
52. S. Spencer, S. Kostel Bal, W. Egner, H. Lango Allen, S. I. Raza, C. A. Ma, M. Gurel, Y. Zhang, G. Sun, R. A. Sabroe, D. Greene, W. Rae, T. Shahin, K. Kania, R. C. Ardy, M. Thian, E. Staples, A. Pecchia-Bekkum, W. P. M. Worrall, J. Stephens, M. Brown, S. Tuna, M. York, F. Shackley, D. Kerrin, R. Sargur, A. Condliffe, H. N. Tipu, H. S. Kuehn, S. D. Rosenzweig, E. Turro, S. Tavare, A. J. Thrasher, D. I. Jodrell, K. G. C. Smith, K. Boztug, J. D. Milner, J. E. D. Thaventhiran, Loss of the interleukin-6 receptor causes immunodeficiency, atopy, and abnormal inflammatory responses. *J. Exp. Med.* **216**, 1986–1998 (2019).
53. A. Dobin, C. A. Davis, F. Schlesinger, J. Drenkow, C. Zaleski, S. Jha, P. Batut, M. Chaisson, T. R. Gingeras, STAR: Ultrafast universal RNA-seq aligner. *Bioinformatics* **29**, 15–21 (2013).
54. T. Stuart, A. Butler, P. Hoffman, C. Hafemeister, E. Papalexi, W. M. Mauck III, Y. Hao, M. Stoeckius, P. Smibert, R. Satija, Comprehensive integration of single-cell data. *Cell* **177**, 1888–1902.e21 (2019).
55. C. S. McGinnis, L. M. Murrow, Z. J. Gartner, DoubletFinder: Doublet detection in single-cell RNA sequencing data using artificial nearest neighbors. *Cell Syst* **8**, 329–337.e4 (2019).
56. A. Gayoso, J. Shor, JonathanShor/DoubletDetection: Doubletdetection v3.0 (Zenodo, 2020); http://doi.org/10.5281/zenodo.4359992.
57. N. J. Bernstein, N. L. Fong, I. Lam, M. A. Roy, D. G. Hendrickson, D. R. Kelley, Solo: Doublet identification in single-cell RNA-seq via semi-supervised deep learning. *Cell Syst.* **11**, 95–101.e5 (2020).
58. X. Huang, Y. Huang, Cellsnp-lite: An efficient tool for genotyping single cells. *Bioinformatics* **37**, 4569–4571 (2021).
59. Y. Huang, D. J. McCarthy, O. Stegle, Vireo: Bayesian demultiplexing of pooled single-cell RNA-seq data without genotype reference. *Genome Biol.* **20**, 273 (2019).
60. I. Tirosh, B. Izar, S. M. Prakadan, M. H. Wadsworth II, D. Treacy, J. J. Trombetta, A. Rotem, C. Rodman, C. Lian, G. Murphy, M. Fallahi-Sichani, K. Dutton-Regester, J. R. Lin, O. Cohen, P. Shah, D. Lu, A. S. Genshaft, T. K. Hughes, C. G. Ziegler, S. W. Kazer, A. Gaillard, K. E. Kolb, A. C. Villani, C. M. Johannessen, A. Y. Andreev, E. M. Van Allen, M. Bertagnolli, P. K. Sorger, R. J. Sullivan, K. T. Flaherty, D. T. Frederick, J. Jane-Valbuena, C. H. Yoon, O. Rozenblatt-Rosen, A. K. Shalek, A. Regev, L. A. Garraway, Dissecting the multicellular ecosystem of metastatic melanoma by single-cell RNA-seq. *Science* **352**, 189–196 (2016).
61. L. Abeler-Dorner, A. G. Laing, A. Lorenc, D. S. Ushakov, S. Clare, A. O. Speak, M. A. Duque-Correa, J. K. White, R. Ramirez-Solis, N. Saran, K. R. Bull, B. Moron, J. Iwasaki, P. R. Barton, S. Caetano, K. I. Hng, E. Cambridge, S. Forman, T. L. Crockford, M. Griffiths, L. Kane, K. Harcourt, C. Brandt, G. Notley, K. O. Babalola, J. Warren, J. C. Mason, A. Meeniga,

Downloaded from https://www.science.org at Leiden University on November 20, 2025

N. A. Karp, D. Melvin, E. Cawthorne, B. Weinrick, A. Rahim, S. Drissler, J. Meskas, A. Yue, M. Lux, G. X. Song-Zhao, A. Chan, C. Ballesteros Reviriego, J. Abeler, H. Wilson, A. Przemska-Kosicka, M. Edmans, N. Strevens, M. Pasztorek, T. F. Meehan, F. Powrie, R. Brinkman, G. Dougan, W. Jacobs Jr., C. M. Lloyd, R. J. Cornall, K. J. Maloy, R. K. Grencis, G. M. Griffiths, D. J. Adams, A. C. Hayday, High-throughput phenotyping reveals expansive genetic and structural underpinnings of immune variation. *Nat. Immunol.* **21**, 86–100 (2020).

62. M. D. Muzumdar, B. Tasic, K. Miyamichi, L. Li, L. Luo, A global double-fluorescent Cre reporter mouse. *Genesis* **45**, 593–605 (2007).
63. Y. Perez-Riverol, J. Bai, C. Bandla, D. García-Seisdedos, S. Hewapathirana, S. Kamatchinathan, D. J. Kundu, A. Prakash, A. Frericks-Zipper, M. Eisenacher, M. Walzer, S. Wang, A. Brazma, J. A. Vizcaíno, The PRIDE database resources in 2022: A hub for mass spectrometry-based proteomics evidences. *Nucleic Acids Res.* **50**, D543–d552 (2022).
64. D. Taliun, D. N. Harris, M. D. Kessler, J. Carlson, Z. A. Szpiech, R. Torres, S. A. G. Taliun, A. Corvelo, S. M. Gogarten, H. M. Kang, A. N. Pitsillides, J. LeFaive, S. B. Lee, X. Tian, B. L. Browning, S. Das, A. K. Emde, W. E. Clarke, D. P. Loesch, A. C. Shetty, T. W. Blackwell, A. V. Smith, Q. Wong, X. Liu, M. P. Conomos, D. M. Bobo, F. Aguet, C. Albert, A. Alonso, K. G. Ardlie, D. E. Arking, S. Aslibekyan, P. L. Auer, J. Barnard, R. G. Barr, L. Barwick, L. C. Becker, R. L. Beer, E. J. Benjamin, L. F. Bielak, J. Blangero, M. Boehnke, D. W. Bowden, J. A. Brody, E. G. Burchard, B. E. Cade, J. F. Casella, B. Chalazan, D. I. Chasman, Y. I. Chen, M. H. Cho, S. H. Choi, M. K. Chung, C. B. Clish, A. Correa, J. E. Curran, B. Custer, D. Darbar, M. Daya, M. de Andrade, D. L. DeMeo, S. K. Dutcher, P. T. Ellinor, L. S. Emery, C. Eng, D. Fatkin, T. Fingerlin, L. Forer, M. Fornage, N. Franceschini, C. Fuchsberger, S. M. Fullerton, S. Germer, M. T. Gladwin, D. J. Gottlieb, X. Guo, M. E. Hall, J. He, N. L. Heard-Costa, S. R. Heckbert, M. R. Irvin, J. M. Johnsen, A. D. Johnson, R. Kaplan, S. L. R. Kardia, T. Kelly, S. Kelly, E. E. Kenny, D. P. Kiel, R. Klemmer, B. A. Konkle, C. Kooperberg, A. Kottgen, L. A. Lange, J. Lasky-Su, D. Levy, X. Lin, K. H. Lin, C. Liu, R. J. F. Loos, L. Garman, R. Gerszten, S. A. Lubitz, K. L. Lunetta, A. C. Y. Mak, A. Manichaikul, A. K. Manning, R. A. Mathias, D. D. McManus, S. T. McGarvey, J. B. Meigs, D. A. Meyers, J. L. Mikulla, M. A. Minear, B. D. Mitchell, S. Mohanty, M. E. Montasser, C. Montgomery, A. C. Morrison, J. M. Murabito, A. Natale, P. Natarajan, S. C. Nelson, K. E. North, J. R. O'Connell, N. D. Palmer, N. Pankratz, G. M. Peloso, P. A. Peyser, J. Pleiness, W. S. Post, B. M. Psaty, D. C. Rao, S. Redline, A. P. Reiner, D. Roden, J. I. Rotter, I. Ruczinski, C. Sarnowski, S. Schoenherr, D. A. Schwartz, J. S. Seo, S. Seshadri, V. A. Sheehan, W. H. Sheu, M. B. Shoemaker, N. L. Smith, J. A. Smith, N. Sotoodehnia, A. M. Stilp, W. Tang, K. D. Taylor, M. Telen, T. A. Thornton, R. P. Tracy, D. J. Van Den Berg, R. S. Vasan, K. A. Viaud-Martinez, S. Vrieze, D. E. Weeks, B. S. Weir, S. T. Weiss, L. C. Weng, C. J. Willer, Y. Zhang, X. Zhao, D. K. Arnett, A. E. Ashley-Koch, K. C. Barnes, E. Boerwinkle, S. Gabriel, R. Gibbs, K. M. Rice, S. S. Rich, E. K. Silverman, P. Qasba, W. Gan, NHLBI Trans-Omics for Precision Medicine (TOPMed) Consortium, G. J. Papanicolaou, D. A. Nickerson, S. R. Browning, M. C. Zody, S. Zollner, J. G. Wilson, L. A. Cupples, C. C. Laurie, C. E. Jaquish, R. D. Hernandez, T. D. O'Connor, G. R. Abecasis, Sequencing of 53,831 diverse genomes from the NHLBI TOPMed Program. *Nature* **590**, 290–299 (2021).
65. J. Vandesompele, K. De Preter, F. Pattyn, B. Poppe, N. Van Roy, A. De Paepe, F. Speleman, Accurate normalization of real-time quantitative RT-PCR data by geometric averaging of multiple internal control genes. *Genome Biol.* **3**, RESEARCH0034 (2002).
66. P. Lobachevsky, L. Woodbine, K. C. Hsiao, S. Choo, C. Fraser, P. Gray, J. Smith, N. Best, L. Munforte, E. Korneeva, R. F. Martin, P. A. Jeggo, O. A. Martin, Evaluation of severe combined immunodeficiency and combined immunodeficiency pediatric patients on the basis of cellular radiosensitivity. *J. Mol. Diagn.* **17**, 560–575 (2015).
67. Y. Xing, X. Wang, S. C. Jameson, K. A. Hogquist, Late stages of T cell maturation in the thymus involve NF-κB and tonic type I interferon signaling. *Nat. Immunol.* **17**, 565–573 (2016).
68. Y. Choi, A. P. Chan, PROVEAN web server: A tool to predict the functional effect of amino acid substitutions and indels. *Bioinformatics* **31**, 2745–2747 (2015).
69. Y. Itan, L. Shang, B. Boisson, M. J. Ciancanelli, J. G. Markle, R. Martinez-Barricarte, E. Scott, I. Shah, P. D. Stenson, J. Gleeson, D. N. Cooper, L. Quintana-Murci, S. Y. Zhang, L. Abel, J. L. Casanova, The mutation significance cutoff: Gene-level thresholds for variant predictions. *Nat. Methods* **13**, 109–110 (2016).
70. J. M. Schwarz, C. Rodelsperger, M. Schuelke, D. Seelow, MutationTaster evaluates disease-causing potential of sequence alterations. *Nat. Methods* **7**, 575–576 (2010).
71. L. Wiel, C. Baakman, D. Gilissen, J. A. Veltman, G. Vriend, C. Gilissen, MetaDome: Pathogenicity analysis of genetic variants through aggregation of homologous human protein domains. *Hum. Mutat.* **40**, 1030–1038 (2019).
72. N. L. Sim, P. Kumar, J. Hu, S. Henikoff, G. Schneider, P. C. Ng, SIFT web server: Predicting effects of amino acid substitutions on proteins. *Nucleic Acids Res.* **40**, W452–W457 (2012).

Acknowledgments: For their contributions to data generation and processing, we thank colleagues within the core facilities teams at both Newcastle University (Bioimaging, Flow Cytometry, Genomics, Comparative Biology Centre) and the Wellcome Sanger Institute (Sequencing, Cellular Genetics, Informatics). We thank J. Nsengimana for expert review of statistical approaches. We also acknowledge S. Teichmann and M. Haniffa for sharing raw data generated in their groups at the Wellcome Sanger Institute and Newcastle University Translational and Clinical Research Institute. We thank L. Bossini-Castillo and S. Navaneethan for the contributions to data generation and analysis. We are grateful to patients and their families, clinical teams, and the laboratories of the Integrated Laboratory Medicine Directorate, Newcastle upon Tyne Hospitals NHS Foundation Trust. **Funding:** This research was funded in part by the Wellcome Trust. Grants supporting this work were as follows: Wellcome Trust grant 207556/Z/17/Z (to S.H.), Wellcome Multiuser Equipment grant 212947/Z/187 (to M.T. and S.H.), Wellcome Trust grants WT206194 and 220540/Z/20/A (to G.T.), Wellcome Trust grants WT098051 and WT206194 (to D.J.A.), Sir Jules Thorn Charitable Trust Biomedical Award 12/JTA (to S.H.), Medical Research Council (UK) grant MR/T029765/1 (to G.A.), and National Human Genome Research Institute grant 5U54HG006542 through the Baylor-Hopkins Center for Mendelian Genomics (to A.S.-P.). **Author contributions:** Clinical care: H.C.E., A.S.-P., A.R.G., and S.H. Conceptualization: R.C., I.S.v.d.L., J.D.P.W., D.J.S., K.R.E., A.S.-P., A.R.G., G.T., and S.H. Data curation: R.C., E.L., I.S.v.d.L., J.S.S., J.D.P.W., A.G., F.L., J.L.M.-R., E.R.R.-M., S.E., K.R.E., A.S.-P., and A.L. Formal analysis: R.C., E.L., I.S.v.d.L., J.S.S., J.D.P.W., K.D.J., H.G., E.R.R.-M., K.R.E., and A.L. Funding acquisition: A.S.-P., M.T., D.J.A., G.A., G.T., and S.H. Investigation: R.C., I.S.v.d.L., J.S.S., J.D.P.W., K.D.J., H.I., A.G., F.L., L.W., H.L., V.P., and K.S. Methodology: R.C., I.S.v.d.L., E.J.R., and D.J.A. Resources: E.J.R., H.L., D.D., M.P., E.P., J.B., A.J.M., L.H., M.v.d.B., A.R.G., D.J.A., and S.H. Supervision: P.J., A.J.M., M.v.d.B., M.T., D.J.A., G.A., A.L., G.T., and S.H. Visualization: R.C., E.L., I.S.v.d.L., J.S.S., J.D.P.W., K.D.J., H.G., J.L.M.-R., K.R.E., and A.L. Writing—original draft: R.C., E.L., I.S.v.d.L., J.S.S., A.L., G.T., and S.H. Writing—review and editing: All authors. **Competing interests:** E.J.R. is an employee at LGC ASSURE. The authors declare that they have no other competing interests. **Data and materials availability:** The mouse strain created for this work, on the C57BL/6NTac/USA background, can be obtained from the European Mouse Mutant Archive with accession number 13836 (full allele name: *Nudcd3*$^{em1(IMPC)Wtsi}$). All data and code with the exception of patient DNA sequencing data are included within this paper or are deposited in data repositories. Exome sequencing data are only available to vetted researchers (and not to the broader public) via a data transfer agreement. The human scRNA-seq data have been deposited to ArrayExpress with accession number E-MTAB-12283. The mass spectrometry proteomics data have been deposited to the ProteomeXchange Consortium via the PRIDE (*63*) partner repository with the dataset identifier PXD035840. The mouse TCR/BCR sequencing data have been deposited to European Nucleotide Archive with the project identifier PRJEB55545. All other data are available in the main text or the Supplementary Materials. Tabulated underlying data for all figures can be found in data S4. All raw immunoblot data exported from LI-COR Image Studio software version 5.2.5 as Image Studio Zip File format can be found in data S5. For the purpose of open access, the author has applied a CC BY public copyright license to any author-accepted manuscript version arising from this submission.

Submitted 24 August 2022
Resubmitted 30 August 2023
Accepted 24 April 2024
Published 24 May 2024
10.1126/sciimmunol.ade5705

Downloaded from https://www.science.org at Leiden University on November 20, 2025